High-resolution description of the hantavirus surface glycoprotein lattice and its membrane fusion control mechanism

Alexandra Serris[1], Robert Stass[2], Eduardo A. Bignon[3], Nicolás A. Muena[3], Jean-Claude Manuguerra[4], Rohit K. Jangra[5], Sai Li[2,9], Kartik Chandran[5], Nicole Tischler[3,6], Juha T. Huiskonen[2,7,8], Felix A. Rey[1#], Pablo Guardado-Calvo[1#]

1. Institut Pasteur, Structural Virology Unit and CNRS UMR3569, Paris, France.
2. Division of Structural Biology, Wellcome Centre for Human Genetics, University of Oxford, Roosevelt Drive, Oxford OX3 7BN, UK
3. Fundación Ciencia & Vida, Molecular Virology Laboratory, Santiago, Chile
4. Institut Pasteur, Paris, France.
5. Department of Microbiology and Immunology, Albert Einstein College of Medicine, New York, NY, USA
6. Universidad San Sebastián, Santiago, Chile
7. Helsinki Institute of Life Science HiLIFE, Viikinkaari 1, 00014, University of Helsinki, Helsinki, Finland
8. Research Programme in Molecular and Integrative Biosciences, Faculty of Biological and Environmental Sciences, Viikinkaari 1, 00014, University of Helsinki, Helsinki, Finland
9. School of Life Science, Tsinghua University, Beijing, China

Correspondence: rey@pasteur.fr (Lead contact), guardado@pasteur.fr

ABSTRACT

Hantaviruses are rodent-borne viruses causing serious zoonotic outbreaks worldwide for which no treatment is available. The hantavirus particles are pleomorphic and display a characteristic square surface lattice. The envelope glycoproteins Gn and Gc form heterodimeric protomers associated into tetrameric spikes, the lattice building blocks. The glycoproteins, which are the sole targets of neutralizing antibodies, drive virus entry via receptor-mediated endocytosis and endosomal membrane fusion. Here we describe the high-resolution X-ray structures of the Gn head / Gc heterodimer, and of the homotetrameric Gn base. Docking them into an 11.4 Å resolution cryo-electron tomography map of the hantavirus surface accounted for the complete extracellular portion of the viral glycoprotein shell and provided unprecedented detail of the surface organization of a pleomorphic virus. These results, which further revealed an in-built mechanism controlling Gc membrane-insertion for fusion, pave the way for immunogen design to protect against pathogenic hantaviruses

INTRODUCTION

Rodent-borne hantaviruses form a close group of viruses distributed worldwide, classified as Old World and New World hantaviruses (OWHs and NWHs) based on their geographical distribution and natural reservoirs (Jonsson et al., 2010). They cause life-threatening zoonotic outbreaks of severe pulmonary disease (NWHs) and of hemorrhagic fever with renal syndrome (OWHs). Despite the severity of these diseases, no efficient treatment is available. Inhalation of aerosols contaminated with infected rodent excreta is the major route of transmission, but person-to-person transmission of a pulmonary syndrome caused by Andes hantavirus (ANDV) has also been reported (Martinez et al., 2005; Padula et al., 1998; Pizarro et al., 2019). NWHs therefore have the potential to adapt human-to-human air-borne transmission routes, increasing their epidemic potential.

The *Hantaviridae* constitute one of twelve families of segmented negative-strand RNA viruses comprised in the recently established *Bunyavirales* order (Maes et al., 2019). As in most other members of this order (generically termed bunyaviruses), the viral genome is composed of three segments, (small, medium and large) of negative-polarity, single-stranded RNA. The medium (M) segment encodes a polyprotein precursor that is matured in the ER by signalase cleavage to generate two envelope glycoproteins, Gn and Gc (Figure 1A) (Lober et al., 2001). Gn interacts co-translationally with the membrane fusion protein Gc, maintaining it in a metastable pre-fusion conformation within a Gn/Gc heterodimer. The protomers further associate into $(Gn/Gc)_4$ tetrameric spikes that are transported to the site of particle morphogenesis, the Golgi apparatus or the plasma membrane depending on the virus (Cifuentes-Munoz et al., 2014). The lateral interactions between adjacent spikes are believed to induce the required membrane curvature required for budding of nascent virions (Huiskonen et al., 2010). Hantavirus particles are internalized into target cells by receptor-mediated endocytosis, with the glycoprotein shell reacting to the acidic endosomal pH to drive the fusion of viral and cellular membranes through a conformational change of Gc (Acuna et al., 2015; Chiang et al., 2016; Cifuentes-Munoz et al., 2011; Jin et al., 2002; Mittler et al., 2019; Ramanathan and Jonsson, 2008; Rissanen et al., 2017).

The X-ray structures of the isolated Gn "head" (Gn^H, comprising the N-terminal 2/3rd of the ectodomain) (Li et al., 2016; Rissanen et al., 2017) and of the Gc ectodomain (Guardado-Calvo et al., 2016; Willensky et al., 2016) of Puumala (PUUV) and Hantaan (HNTV) hantaviruses (both OWHs) have been reported. Gc was shown to feature the three characteristic β-sheet rich domains (I, II and III) observed in the class II fusion proteins of the flaviviruses (Rey et al., 1995), alphaviruses (Lescar et al., 2001) and phleboviruses (Dessau and Modis, 2013). The central domain I is a β-sandwich composed of an inner ($B_0I_0H_0G_0$) and an outer ($C_0D_0E_0F_0$) β-sheet ("inner" and "outer" refer to their orientation in the postfusion trimer (Guardado-Calvo et al., 2016)). The D_0E_0 and H_0I_0 connections between adjacent

β-strands form long excursions (amino acids 713–804 and 840–949) projecting from one end of the domain I β-sandwich to form the elongated domain II. A flexible linker connects the opposite end of the domain I β-sandwich to the C-terminal immunoglobulin superfamily (IgS) domain III (aa 973–1,061), which in turn connects to the C-terminal transmembrane (TM) anchor (aa 1,108–1,130) via an extended segment termed "stem". Domain II is composed of a domain I-proximal sub-domain made of a highly twisted β-sheet (*klaefg*, Figure 1), and a distal "tip" subdomain composed of the elongated *bdc* β-sheet packing against the *ij* β-hairpin. The tip exposes the target membrane insertion surface (TMIS) at the distal end of the protein. Unlike the class II fusion proteins from the flaviviruses and alphaviruses, in which the TMIS is composed of a single loop (the *cd* loop, also termed the "fusion loop"), hantavirus Gc has a tripartite TMIS composed of residues in loops *bc* (Tyr739), *cd* (Trp766) and *ij* (Phe900) (Guardado-Calvo et al., 2016; Guardado-Calvo and Rey, 2017). The available structural snapshots of Gc show a monomer in an extended conformation stabilized by an antibody bound to the domain II tip, and a Gc trimer in the characteristic post-fusion "hairpin" conformation observed in other viral class II fusion proteins (Bressanelli et al., 2004; Gibbons et al., 2004; Luca et al., 2013; Modis et al., 2004).

The hantavirus square surface lattice was initially observed by negative stain electron microscopy (Martin et al., 1985) and later characterized by cryo-electron tomography (cET) studies on particles of the OWH Tula virus (Huiskonen et al., 2010) and by single particle averaging of the spikes on HTNV virions (Battisti et al., 2011). The cET studies showed pleomorphic particles with locally ordered lattices of tetrameric $(Gn/Gc)_4$ spikes coating the viral membrane. A model for the organization of Gn and Gc in these lattices was proposed (Hepojoki et al., 2010) in which Gn was located at the spike center and Gc at the periphery, respectively making intra- and inter-spike contacts. This model was in line with structural studies combining cET, sub-tomogram averaging (STA) and the X-ray structure of the isolated PUUV Gn^H (Li et al., 2016). It was further supported by functional studies confirming that the crystallographic 2-fold contacts made by HTNV Gc monomers (Guardado-Calvo et al., 2016) recapitulate the lateral interactions between spikes on particles (Bignon et al., 2019). Despite these advances, the actual organization of the spike and the molecular interactions between Gn and Gc within the spike have remained elusive.

Here, we report the X-ray structure of the metastable pre-fusion Gn^H/Gc heterodimers of ANDV and Maporal virus (MAPV, a NWH closely related to ANDV) to 2.2 and 3.2 Å resolution, respectively. The ANDV complex required a stabilizing mutation in Gc to avoid a spontaneous conformational change into the post-fusion conformation despite the presence of Gn^H. We also describe the X-ray structure of the Gn base (Gn^B, the C-terminal third of the ectodomain) to 1.9 Å, showing that it forms a tight tetramer. These structures docked unambiguously into a 11.4 Å resolution cET map of the Tula virus Gn/Gc spikes, confirming that the Gn^H/Gc and Gn^B conformations captured

in the crystals indeed correspond to their active form in the spikes of infectious hantavirus particles and providing a complete model for the surface glycoprotein lattice. Functional studies by targeted mutagenesis further confirmed the detailed picture of the tetrameric spike organization as well as the lateral interactions between spikes. The Gn^H/Gc structure also revealed that, unlike other class II fusion proteins, Gn^H release at acid pH induces a conformational change of the domain II tip to form the TMIS for insertion into the endosomal membrane.

RESULTS

Structural characterization of the hantavirus glycoproteins

We produced the soluble ectodomains of the hantavirus Gn^H/Gc heterodimer using a single chain construct in which a soluble linker bypassed the Gn TM and intraviral/cytosolic segments to connect directly to the Gc N-terminus (Figures 1A and B). Only constructs in which the conserved Gn^B region of the ectodomain was removed (orange in Figures 1 and S1A) – a region that was also absent in the reported structures of isolated Gn^H (Li et al., 2016; Rissanen et al., 2017) – yielded enough soluble protein. Our final constructs thus included aa 23–374 of Gn (corresponding to Gn^H) and 652–1107 of Gc (ANDV polyprotein numbering), corresponding to the complete Gc ectodomain. Of the various hantavirus orthologs we tested, only constructs from the related New World hantaviruses ANDV and MAPV (accession numbers NP_604472.1 and YP_009362281, respectively) yielded enough protein for structural studies (an aa sequence alignment of selected hantavirus Gn and Gc orthologs is provided in Figure S1). We purified the proteins to homogeneity from the supernatant of stably transfected *Drosophila* Schneider 2 (S2) cells. Upon proteolytic removal of the linker using thrombin, we obtained monoclinic crystals for MAPV Gn^H/Gc diffracting to 2.2 Å resolution and rhombohedral crystals for ANDV Gn^H/Gc diffracting to 2.6 Å (Table 1) and determined the structures by molecular replacement. Both displayed Gn^H attached to the tip of Gc (Figure 1B), but showed two strikingly different overall conformations, with Gc in the ANDV Gn^H/Gc structure forming the characteristic post-fusion trimer despite having Gn^H bound. Using the same approach, we produced in parallel the C-terminal region of the Gn ectodomain (Gn^B, aa. 375–484) from ANDV. Gn^B crystallized in an orthorhombic and in a tetragonal space group at acidic and neutral pH, respectively. We obtained an iodide derivative of the tetragonal crystals that allowed the structure determination by single wavelength anomalous dispersion (SAD) to 2.4 Å resolution. We used the resulting atomic model for molecular replacement to solve the structure in the orthorhombic crystals and refined it to 1.9 Å resolution (Table 1). Both crystals showed an identical intertwined Gn^B tetramer containing an N-terminal β-sandwich (aa 379–446) featuring an IgS fold, followed by a C-terminal α-helical hairpin (Figure 1C).

The Gn^H/Gc heterodimer features Gc in the pre-fusion conformation

To facilitate validation of the X-ray structures and the subsequent modeling of the spike, we improved the cET map of the Tula hantavirus Gn/Gc *in situ* tetramer reported earlier at 16 Å resolution (Li et al., 2016). We increased the resolution of the map to 11 Å by using a larger dataset combined with strategies for removing noise and accounting for conformational flexibility of the spike itself. These improvements included restricting the dataset to only use particles that form regular patches on the virion surface and 3D classification. The correct handedness of the map was established by including human papillomavirus capsids in the sample as reference, showing that the hand of the previously reported map was inverted (Figure S2A-F). At 11-Å resolution, the cET map of Tula virus is representative of prefusion spikes in ANDV and in hantaviruses in general due to high sequence identity amongst the glycoproteins (e.g. Tula virus Gn and Gc display 63% and 73% amino acid sequence identity with their ANDV counterparts, respectively). When we docked the 2.2 Å resolution MAPV Gn^H/Gc structure (Figure 1B, left panel) into the cET map as a rigid-body (Figures S3A, S3D and Table 2), the overall fit was satisfying, although domain III was partially out of cET density. The 2.6 Å resolution structure of ANDV Gn^H/Gc, did not fit the cET map, as expected since it features Gc in the post-fusion conformation.

In order to trap the ANDV heterodimer in its pre-fusion form, we inspected the structure of the post-fusion trimer in order to find potential mutations destabilizing the trimer. Similar approaches have been used to stabilize the pre-fusion conformation of some of the class I fusion proteins (Krarup et al., 2015; Pallesen et al., 2017; Rutten et al., 2020). We noted that the His953 side chain is involved in a tight network of polar interactions with the side chains of Asp679, Lys833 and Asn955 at the center of the Gc trimer. We thus introduced the H953F mutation, as the bulkier phenylalanine side chain cannot make the same interactions. Furthermore, the H953F mutant had been shown not to interfere with budding of ANDV VLPs (Bignon et al., 2019), indicating that it should not affect the Gc pre-fusion conformation. The ANDV Gn^H/Gc H953F mutant yielded hexagonal crystals diffracting to 3.2 Å resolution (Table 1), in which Gn^H/Gc adopted an organization very close to that of wild-type MAPV Gn^H/Gc (Figure S3B). The two complexes could be aligned with a root mean square deviation (rmsd) of 5.7 Å between all pairs of equivalent Cα atoms, although the individual domains superposed to about 0.5 Å rmsd. The two structures differed essentially at the level of the hinge of Gc domain II (in the *klaefg* β-sheet, Figures 1 and 3), at its domain I proximal end (Figure S3F). This region has been shown to adopt variable conformations in other class II fusion proteins, for instance in the envelope proteins of dengue virus (Zhang et al., 2004) (a flavivirus) and in the rift Valley fever virus (Halldorsson et al., 2018) (a phlebovirus). When we docked the atomic model of ANDV Gn^H/Gc H953F into the cET map as a single rigid body, the altered conformation at the hinge brought domain III to fit well within cET density (Figure S3E). Accordingly, the correlation coefficient (0.88) between the cET density and the

resulting model, and the percentage of atoms inside density (88.9%) were higher than those obtained with the structure of the MAPV Gn^H/Gc (0.87 and 84.6%, respectively, Table 2). Taken together, these results confirmed that the complex trapped in the MAPV Gn^H/Gc and ANDV Gn^H/Gc H953F crystals displayed Gc in a genuine pre-fusion conformation.

To further validate that the interface observed in the crystals indeed corresponds to that of Gn/Gc heterodimers at the viral surface, we used the DbD2 server (Craig and Dombkowski, 2013) to identify pairs of residues interfacing each other at the Gn^H/Gc contact surface with favorable geometry to form an inter-chain disulfide bond when mutated to cysteine (Figure 1D, left panel). We monitored the formation virion-like particles (VLPs) by introducing the double mutations into a full-length ANDV Gn/Gc construct that yields VLPs. We found that mutants H294C/T734C, T99C/P774C and N94C/V776C (the numbering corresponds to the polyprotein precursor, Figure S1) did not interfere with efficient VLP formation as compared to the wild type construct. SDS-PAGE analysis (Figure 1D, right panel) showed that while Gn and Gc from wild type VLPs migrated as monomers (at ~70 and ~55 kDa, respectively) under both reducing and non-reducing conditions, Gn and Gc from VLPs formed by the double mutants migrated similarly only upon reduction. In a non-reducing gel, however, these mutants ran as a single band migrating as a ~130 kDa form that was recognized by anti-Gn and by anti-Gc antibodies. The presence of this species, which is absent in wild type VLPs and which dissociates into Gn and Gc monomers by addition of a reducing agent, indicates the presence of covalently linked heterodimers on the particles. In conclusion, the match to the cET density and the mutagenesis results strongly support the interpretation that the Gn^H/Gc complex observed in the crystals reflects interactions present on the viral particles.

An overall model of the spike and the surface glycoprotein lattice

The 3.2Å resolution X-ray structure of ANDV Gn^H/Gc H953F docked as rigid-body into the asymmetric unit of the cET was used to generate its immediate neighbors by applying four-fold symmetry around the central spike axis using Chimera (Pettersen et al., 2004). The resulting $(Gn^H/Gc)_4$ tetramer filled most of the spike, but left an unaccounted density volume at the membrane-proximal side, where most of the four-fold contacts appear to take place. In the spike model, the C-terminal end of the crystallized Gn^H construct pointed into this unoccupied density, strongly suggesting that it should correspond to Gn^B (Figure 1A). Indeed, the X-ray structure of the Gn^B tetramer nicely fitted as a rigid body into this volume of the map (Figures 2A-D, and Table 2), confirming that Gn^B contributes the most to the intra-spike tetrameric contacts. The separate docking of the Gn^H/Gc heterodimer and the Gn^B tetramer thus yielded a complete model for the external region of the hantavirus spike. The C-terminal end of Gn^B points to a transmembrane segment, the density of which is resolved in the 11Å resolution cET map. The N-terminus of Gn^H, in contrast, projects at the top of the spike (Figure 2),

exposed to solvent and compatible with the reported N-terminal fusion of heterologous sequences that are tolerated and accessible on particles (Jangra et al., 2018).

The model for the spike tetramer further revealed that the *N*-glycans attached to Asn402 and to Asn930 map to internal cavities of the spike (Figure 2) and appear to play a stabilizing structural role, despite the mobility of the sugar chains. Mutations knocking out glycosylation at these sites were indeed shown to result in Gn/Gc spike complexes that reach the Golgi apparatus efficiently, but are not recognized by certain conformational antibodies (Shi and Elliott, 2004). These observations indicate that the integrity of the $(Gn/Gc)_4$ tetramer may be compromised by the absence of the internal glycan chains, which appear to form a scaffold underneath the spike surface. The arrangement of Gn and Gc in the spike is also in line with the observation that the *N*-linked glycans are of the high-mannose type (Antic et al., 1992; Schmaljohn et al., 1986; Shi and Elliott, 2004), as they appear sterically protected from further modification in the Golgi. Some hantaviruses, such as Dobrava, Hantaan and Thottapalayam viruses, display additional *N*-glycosylation motifs in Gn. These additional sites are however predicted to be exposed at the top of the spike and would project the sugar chains to solvent at the very top, where they would be susceptible to modification in the Golgi to the complex form.

The adjacent spikes in the hantavirus surface lattice were similarly generated by local rigid body fitting. The resulting lattice model confirmed that the $(Gn/Gc)_4$ spikes are formed essentially by Gn:Gn contacts, and the lattice is formed by inter-spike Gc:Gc contacts. The inferred homodimeric Gc:Gc interface is similar to that observed previously in a crystallographic dimer of HNTV Gc crystallized at neutral pH in complex with an antibody (PDB:5LJY), (Guardado-Calvo et al., 2016), with an additional contribution from the Gc N-terminal segment, which augments the inner sheet by contributing an additional β-strand (A'_0 strand, in pink in Figure 3B). The relatively small buried surface area (550 $Å^2$ per protomer) suggests that a certain degree of rocking about the inter-spike contacts is allowed, consistent with the pleomorphic nature of the particles. Imposing the exact interactions observed in the crystallographic Gc dimer to the inter-spike contacts resulted in slightly reduced fitting scores in comparison to fitting the individual Gn/Gc protomers (Table 2), possibly because there are more degrees of freedom that could artificially increase the scores at this resolution. Overall, our results are in line with the previously reported data showing that mutations guided by the crystallographic Gc dimer interface interfere with spike-spike interactions and block particle assembly (Bignon et al., 2019).

The model derived previously by docking the X-ray structure of PUUV Gn^H into the 16-Å resolution Tula virus cET map (Li et al., 2016) was overall consistent with the new model, with Gn at the center and making 4-fold contacts in the spike, and Gc making inter-spike contacts. The reason is that at 16 Å resolution the individual spikes are essentially centrosymmetric. The surface lattice,

however, is not, but there was no attempt to dock Gc in that model. A detailed comparison showed that there is actually a different orientation of Gn^H in the new spike model, which leads to different exposed surfaces and inter-protomer contacts (Figure S2G-H). We used the new model for the hantavirus surface glycoprotein lattice to map the available data – most often Pepscan data (Koch et al., 2003) (Heiskanen et al., 1999) - on sites recognized by monoclonal antibodies (mAb) targeting different human pathogenic hantaviruses. Most of these data consist of peptides mapping to different regions of the glycoprotein, often distal in the primary sequence. We found that the reported peptides reactive with individual Mabs are brought together in the atomic model to form a continuous patch at the particle surface, compatible with the location of the epitope for each Mab. Some of the peptides belong to different protomers, but cluster at Gn:Gn and Gc:Gc contact regions at the lattice surface (Figures S2G-I).

The Gn/Gc interface

The structures of the Gn^H/Gc heterodimer described here (including the ANDV $(Gn^HGc)_3$ trimer) show the Gn^H moiety making extensive interactions with Gc domain II (Figures 3 and S3A-C). The Gn^H/Gc interface buries about 1,950–2,050 $Å^2$ per protomer, of which roughly 20% involve contacts with *N*-linked glycans. The contact regions between the two protomers are mediated via conserved surface patches in both glycoproteins (Figure S3G). The Gc prefusion conformation is stabilized by interactions between domain III and the domain I outer sheet, which is augmented by an additional β-strand (K_0, aa 1,077–1,082) formed by residues belonging to the stem region (Figure 3B), and a Gc N-terminal extension (the "N-tail", aa 652–668 - "extension" with respect to other class II fusion proteins). Three conserved aromatic side chains in these two segments, (W660, H665, Y1080) make important side chain contributions by forming a platform interfacing with domain III. The N-tail makes an arch that surrounds domain I, forming an additional short β-strand (A'_0) that augments the domain I inner sheet (Figure 3B). The contribution of the stem and the N-tail to the pre-fusion conformation of domain I are features that have not been described for other viral class II fusion proteins. The previously reported structure of monomeric HTNV Gc at neutral pH, interpreted as displaying a potential "pre-fusion" conformation, had been obtained after controlled proteolysis that cleaved off the stem, and therefore lacked the K_0 strand (Guardado-Calvo et al., 2016). The N-tail was in turn disordered upstream strand A_0 (aa 669–672). The absence of these contact sites gave rise to a displaced domain III that resulted in a rod-like Gc molecule in which domains II and III lie at the opposite ends of domain I (Figure 3D). This conformation would be compatible with an extended intermediate form of Gc adopted early during the membrane fusion reaction, as observed in other bunyaviruses (Halldorsson et al., 2018).

The Gn^H conformation in the complex is essentially the same as that observed in the structures of isolated Gn^H from PUUV and HTNV reported previously (Li et al., 2016; Rissanen et al., 2017), except for three disordered loops that are involved in interactions with Gc in the heterodimer. Many features of the Gn/Gc complex are reminiscent of the alphavirus p62/E1 glycoprotein heterodimers (Voss et al., 2010). Both p62 and Gn present three IgS domains (termed domains A, B, and C) disposed around a central β-ribbon structure (Figure S4). The β-ribbon consists of a long, twisted β-hairpin encircled by several "arches", which in Gn are more elaborate than in p62, displaying various insertions with additional secondary structure elements. Despite the overall similarity, Gn domains A and B are disposed differently with respect to each other compared to p62 and have developed different insertions into the core domains to interact within the heterodimer. These differences notwithstanding, in both cases they engage domain II of their partner fusion protein by interacting with the *b* strand and the *de* loop, and both have domain C immediately downstream the β-ribbon. Furthermore, the icosahedral alphavirus surface glycoprotein lattice is maintained by intra-spike contacts made exclusively by p62, whereas the inter-spike 2-fold contacts are mediated by E1 only, just as in the Gn/Gc square surface lattice in the hantavirus particle. These similarities indicate that not only that E1 and Gc are homologs but also that Gn is evolutionary related to p62 despite having diverged further in structure.

One of the three main Gn regions contacting Gc is the "η1 loop", centered on a 3/10 helical turn (η1 helix, aa 289–291) in the MAPV structure. This loop encompasses a polypeptide segment (aa 277–299) featuring the highly conserved stretch 281-GEDHD-285 across the *Orthohantavirus* genus (Figures S1, S3H-J and S4). The C-terminal end of the η1 loop forms β-strand A_B running parallel to β-strand *b* of Gc domain II. A second contact site with Gc involves the Gn arch surrounding the β-ribbon (arch1, aa 202–208), which interacts with the *fg* and *kl* loops in the hinge region of Gc domain II (Figure 3B). The third set of important interactions is made by the tip of a long β-hairpin (i1-i2 hairpin, Figures 3C and S4), which stands out as an insertion into Gn domain A. The i1-i2 loop at the tip of this β-hairpin packs against the *cd* and *bc* loops of Gc, and we accordingly term it "capping loop" (aa 88–99). This loop adopts several conformations in the absence of Gc, as shown by the structures of isolated Gn^H crystallized at different pH, none of which corresponds to the conformation seen here in the complex with Gc (Figure S3K). A striking additional inter-chain interaction is mediated by the two Gn conserved glycan chains attached at positions N138 and N350, which embrace the tip of domain II (Figure 3C) respectively interacting with the side chains of Phe900 and Tyr745, both residues forming part of the Gc TMIS. Removal of either of these glycosylation sites in HTNV has been shown to give rise to defects in the intracellular transport of the glycoprotein complex (Shi and Elliott, 2004).

The intra-spike interfaces

Similar to the trimeric alphavirus spike, the intra-spike contacts stabilizing the hantavirus spike mostly involve Gn. There are sparse contacts at the membrane distal side between the conserved GFC β-sheet of domain A and the arch-1 region from the clockwise protomer seen from the top (Figures 4A and 4C). However, most of the four-fold contacts appear to take place at the membrane-proximal side of the spike, and are mediated by the Gn^B moiety (Figures 4B, D, and E). The Gn^B X-ray structure revealed a seven-stranded IgS β-sandwich domain (Gn domain C, aa 379–446) followed by a viral membrane proximal external region (MPER) (Figure 4B) composed of two amphipathic α-helices, which form a disulfide-linked α-helical hairpin. The Gn MPER wraps around domain C from an adjacent protomer (Figure 4B) to make an intertwined, compact tetramer with a large buried surface area (BSA) at the interface (1000 A^2 per protomer distributed equally between both domains). Accordingly, a construct containing only domain C, i.e. lacking the Gn MPER region, behaves in solution as a monomer (data not show). Most of the residues that shape the interface are conserved across hantaviruses (Figure S1). The base of the tetramer exposes a hydrophobic surface composed of 28 conserved hydrophobic residues (seven per protomer, Figure 4B), facing the viral membrane.

The Gn^H/Gc crystals displayed clear density for the Gc stem except for its N-terminal segment (aa 1,063–1,076) between domain III and the K_0 strand (Figure 3B). In the model for the spike, the disordered region appears to enter the cET density volume occupied by Gn^B from a clockwise protomer of the tetramer when looking from the top (Figure 4D). It is possible that this segment of the stem requires Gn domain C to become structured. We note that the crystals of the Gn^B tetramer included a ligand – which was present in both crystal forms and which we interpreted as a short RNA oligonucleotide – inserted in a groove between two Gn^B protomers. This ligand, which copurified with the protein and is not likely to be biologically relevant, revealed nevertheless the existence of a reactive groove along the sides of the Gn^B tetramer, running radially and well placed to accommodate the N-terminal segment of the Gc stem in the context of the spike. The resulting intertwined arrangement of Gc, interacting with two Gn protomers via domain II and the stem, further strengthens the interactions withing the tetrameric spike. In the alphavirus p62/E1 complex, the corresponding region of the E1 stem was also shown to be structured in interaction with p62 domain C (Voss et al., 2010). In this case, however, these contacts are within the same p62/E1 heterodimer, contrary to the cross-Gn/Gc heterodimer of the hantavirus Gc stem.

The C-terminal part of the stem (aa. 1,092–1,107, between the K_0 strand and the TM segment, Figure S1), is also disordered in the Gn^H/Gc crystals. The Psipred server (Buchan and Jones, 2019) predicts this Gc MPER as an amphipathic α-helix that would span the 30-Å distance intervening between the last ordered stem residue in the Gc model and the cET density for the Gc TM segment (Figure 4A). The Gc MPER would lie parallel to - and partially embeded in - the viral membrane outer

leaflet. At 11 Å resolution it is not resolved in the cET map, probably because of the poor density contrast with the electron-rich phosphate groups of the lipid heads (contrary to the TM helices, where the contrast with the aliphatic moiety of the lipids is high). Similar MPERs have been described for other class II fusion proteins just upstream the TM segments, for instance the envelope protein of dengue virus (Zhang et al., 2013), but also for the class I envelope trimer of HIV (Fu et al., 2018) and the class III fusion protein gB of herpes simplex virus (Cooper et al., 2018). We note that mutations in this region, such as S1094L, which would increase the Gc MPER amphipathic character, were reported to increase the infectivity of recombinant vesicular stomatitis virus particles bearing HNTV Gn/Gc glycoproteins (Slough et al., 2019), suggesting that the interaction of the Gc MPER with membranes may affect viral infectivity. Together, the Gn and Gc MPERs appear to form a platform underneath the spike, interfacing with the viral membrane (Figures 4A and E). The compound effect of embedding all or most of these amphipathic helices in the outer leaflet of the lipid bilayer would be expected to significantly affect the curvature of the viral membrane (Martyna et al., 2017).

The fusogenic conformational change of Gc

In order to better understand the structural reorganization that takes place during viral fusion, we also made constructs of the isolated MAPV and ANDV Gc ectodomains, and obtained crystals diffracting to 2.7 and 2.4 Å resolution, respectively (Table 1). The resulting structures revealed Gc in its post-fusion conformation (Figure 5A, central and right panel) even when crystallized at neutral pH, as was the case with the HTNV and PUUV post-fusion Gc trimers reported earlier (Guardado-Calvo et al., 2016; Willensky et al., 2016).

Comparison of the pre- and post-fusion conformations of Gc confirmed that the most conspicuous changes are the drastic relocation of domain III and the stem segment, as well as an altered topology of the β-strands composing the outer and inner sheets of domain I (Figures S5A, and E). Similar changes had been reported for other class II fusion proteins analyzed previously in pre- and post-fusion forms (Guardado-Calvo et al., 2017; Modis et al., 2004; Voss et al., 2010).

Unlike the other class II fusion proteins studied until now, the domain II tip adopts an alternative conformation, stabilized by Gn, in which the TMIS is not formed (Figure 5B). The observed reorganization of the tip mainly affects the *cd* loop, which in the post-fusion form makes an α-helical turn exposing the side chain of Trp766 and burying that of Asn769. By contrast, in the pre-fusion form, the Trp766 side chain is buried and that of Asn769 is exposed to solvent (Figures 5B and S5D). This rearrangement results in a drop of the surface hydrophobicity at this critical membrane-interacting region. The few remaining non-polar side chains exposed after this reorganization are covered by the Gn capping loop, which cloaks Tyr745 in the *bc* loop and part of the *cd* loop. In addition, the N138 glycan makes a stacking interaction with Phe900 of the *ij* loop, which is not exposed either.

What controls the observed reorganization of the tip is unknown, but the unusual carboxylate/carboxylic-acid hydrogen bond between the side chains of the strictly conserved Glu757 and Asp759 (Guardado-Calvo et al., 2016) is likely to play role. We observed that this acidic hydrogen bond is required for structuring the tip of domain II in the post-fusion conformation. The presence of Gn reshapes the *bc* loop such that the neighboring Lys744 makes a hydrogen bond / salt bridge with Asp759, preventing formation of the acidic hydrogen bond and therefore precluding the *cd* loop from exposing Trp766 (Figure S5F). How the changes in the *bc* loop are transmitted to the *cd* and *ij* loops remains an open question.

DISCUSSION

Our study revealed the organization of the hantavirus surface by describing the X-ray structures of ANDV and MAPV Gn^{H}/Gc heterodimer glycoprotein complexes in the prefusion conformation, the conserved tetrameric Gn base of ANDV and their rigid-body fitting into a 11-Å resolution cET map of Tula hantavirus. Given the high amino acid sequence similarity between the envelope glycoproteins, the model presented here is expected to be valid for all hantaviruses. The Gn^{H}/Gc structures revealed the role played by the N-terminal tail and stem of Gc in stabilizing the interaction between domains I and III in the metastable prefusion form. In addition, the effect of Gn in the conformation of the Gc tip revealed the way Gn protects from premature TMIS formation. These features have not been previously observed in other class II fusion proteins. Because the domain II tip displays clear amino acid sequence conservation with its counterpart in nairoviruses and in orthobunyaviruses, the observed protection mechanism is likely to be extrapolated to the fusion machinery of those more distant viruses.

The evolutionary history of the class II fusion proteins remains enigmatic. They have been identified in positive- and in negative-sense ssRNA viruses as well as in multiple and varied eukaryotic organisms where they drive the fusion of gametes and of somatic cells (Fedry et al., 2017; Perez-Vargas et al., 2014). Their complex yet highly conserved 3D fold is strong evidence for common ancestry despite the absence of any remnants of sequence conservation (Modis, 2014). We show here that the similarity in the viral proteins extends beyond the actual fusion effector protein to include the accompanying protein as in the case of the alphaviruses and hantaviruses. Indeed, despite major differences, we found that the overall organization of the hantavirus spike showed unanticipated parallels with that of the alphavirus spike. These include the roles of domains A and C of Gn, which like their counterparts in alphavirus p62 make the intra-spike contacs, and Gc - like its alphavirus E1 counterpart - providing lateral contacts between spikes. The flavivirus example also shows that in some cases, this accompanying prM protein has been substituted during evolution (Li et al., 2008). Yet even

in this case, the accompanying protein binds to the domain II tip by interacting with β-strand *b*, in an apparently universal fashion.

The quasi-atomic model of the spike presented here provides a framework to understand an accumulating body of data on hantavirus biology. The conserved *N*-linked glycans, which were observed to be buried in the spike and which remain high-mannose in released viral particles, are a prime exemplar. Our structures support the hypothesis that the tetrameric spikes form early in the ER, before they are transported to the Golgi apparatus. The sugar chains are then not accessible to the glycosyl transferases that modify the glycan chains, buried within the tetramer. As the sugar chains are buried, they are not used as a shield to evade the immune system as in other viruses, nor as cellular attachment factors as in alphaviruses, flaviviruses or phleboviruses (Watanabe et al., 2019). Rather, the glycans appear to play an intrinsic structural role by forming an internal scaffold.

Previous studies have reported a dynamic behavior of the hantavirus spikes, which exhibit a temperature-dependent equilibrium between two conformational states, which co-exist at physiological temperatures (Bignon et al., 2019), termed “breathing”. The closed form, which is infectious and requires acidic pH to expose the TMIS; and the open form, which exposes the TMIS even at neutral pH but is unable to fuse membranes upon acid-exposure. The structure of the Gn^{H}/Gc heterodimer presented in this manuscript appears to reflect the closed form, since the capping loop partially shields the TMIS and the Trp766 side chain is buried. The open form will probably result from a partial dissociation of the heterodimer, leading to a change in the conformation of the *cd* loop and its interaction with membranes. It has been hypothesized that spike breathing may provide advantages to establish persistent infections in rodents by exposing decoy epitopes that elicit a poorly neutralizing response (Bignon et al., 2019). In line with this hypothesis, neutralizing antibodies isolated from mice (Xu et al., 2002) and bank voles (Lundkvist and Niklasson, 1992), which were respectively immunized with inactivated HNTV and PUUV infected tissues, recognize epitopes occluded in the closed form (Figure S2) but which can be transiently exposed as the spike breaths.

The atomic model of the hantavirus spike now paves the way for the development of novel immunogens. Designing subunit vaccines using the recombinant fusion glycoprotein ectodomain for immunization has been complicated by the spontaneous and irreversible adoption of the post-fusion form, thereby losing the relevant epitopes targeted by neutralizing antibodies. One example is the respiratory syncytial virus (RSV) fusion (F) glycoprotein, which required mutagenesis to stabilize its pre-fusion conformation (Krarup et al., 2015) and expose the right epitopes to elicit strongly neutralizing antibodies. We found a similar situation with ANDV Gn^{H}/Gc complex, and we describe one way of interfering with the adoption of the post-fusion form by introducing the H953F mutation. We have furthermore validated our model for the spike by designing disulfide bridges crosslinking the Gn/Gc protomer, providing a proof-of-principle that such additional stabilization is feasible. Our results make

it now possible to further investigate inter-protomer disulfide bonds to stabilize the overall spike tetramer as a potential next-generation immunogen. As spike "breathing" has been demonstrated in Andes virus and other hantaviruses that cause severe disease in humans, spikes engineered as proposed here should provide superior immunogens for eliciting highly potent neutralizing antibodies targeting the closed form of the spike.

DEPOSITED DATA

The atomic coordinates and structure factors of the X-ray structures have been deposited in the Protein Data Bank (www.pdb.org) with accession codes 6Y5W, 6Y5F, 6Y62, 6Y68, 6Y6Q, 6Y6P, 6YRB, and 6YRQ. The cET map has been deposited in the Electron Microscopy Data Bank (www.ebi.ac.uk/pdbe/emdb/) with accession number EMD-XXXX. Atomic coordinates of the tetrameric spike quasi-atomic model have been deposited in the Protein Data Bank with the accession code XXXX. The previously reported "inverted" map EMD-3364 has been redeposited with accession code EMD-4867.

FIGURE LEGENDS

Figure 1. X-ray structures of the hantavirus glycoproteins. A) Domain organization of the hantavirus M segment. The upper panel shows a diagrammatic representation of the open reading frame (ORF) encoding for the polyprotein precursor to Gn and Gc. The signal sequence is shown in cyan, and the three transmembrane regions present are labelled. The ectodomain of Gc is in yellow and that of Gn in red (Gn^H) and orange (Gn^B) for the head and base portions, respectively. The endodomain and TM segments are in grey. The glycosylated asparagine residues are labeled in green above the ORF. An arrow marks the signalase cleavage site separating Gn from Gc. The lower panel shows a schematic representation of the Gn/Gc heterodimer with the viral membrane drawn as a dashed box and the transmembrane regions as vertical rectangles. The ectodomains of Gn and Gc are colored as in (A), with the N- and C- termini labelled and the *N*-linked glycans indicated with "Y" symbols. B) Structures of the hantavirus Gn^H/Gc heterodimer. The first row shows a diagrammatic representation of the single-chain Gn^H/Gc construct used for crystallization upon thrombin treatment. The second and third rows show two orthogonal views of the MAPV Gn^H/Gc (left), ANDV $(Gn^H/Gc)_3$, (middle) and the ANDV Gn^H/Gc-H953F mutant (right). In the middle panel, the $(Gn^H/Gc)_3$ trimer is shown with the Gc chains in yellow, grey and light-cyan surface representation, and Gn as red ribbons. In the side view (second row of the Figure), the Gn chain was omitted for clarity, and the front Gc chain is shown as ribbons, as in the left and right panels, displayed after structural alignment on domain I. The top view (third row) also shows the glycan chains as green sticks and labeled. The fourth row shows a closeup of the Gn^H/Gc

interface (left panel) marking the location of the engineered inter-chain disulfide bonds (green bars) The right panel shows an SDS-PAGE analysis under reducing and non-reducing conditions of VLPs released into the supernatant of cells expressing wild type ANDV GnGc and the indicated Cys double mutants analyzed by SDS-PAGE in the or presence or not of a reducing agent, as indicated. **C)** Structure of the ANDV Gn^B tetramer in side view (top) and top view (bottom), with one Gn^B chain highlighted in orange. The only N-glycan attached to Gn^B is indicated as green sticks and labelled. Represented in blue is the density corresponding to an omit map contoured at 1.5σ, indicating the site of a molecule bound during production of the protein in S2 cells (see Methods). This density is shown to highlight the location of a reacting groove at the Gn^B surface, which we postulate that in the spike may interact with the Gc stem.

Figure 2. Organization of hantavirus Gn/Gc spikes on virions. A) The hantavirus spike viewed from the top, along the 4-fold axis. The x-ray structures of the ANDV Gn^H/Gc-H953F mutant and of Gn^B (orange) were docked into the cET density. Only one of the four Gn^H/Gc protomers in the spike is colored as in Fig. 1. One protomer of the adjacent spike, related by a 2-fold axis, is highlighted in salmon/blue (respectively for Gn^H and Gc). The symmetry axes are indicated by numbers: the spike's 4-fold axis is perpendicular to the plane of the Figure, and the 2-fold inter-spike axes are slightly tilted. B) Orthogonal view of the spike with the 4-fold axis in the plane of the Figure. The conserved *N*-linked glycans (visible on the spike on the right) are shown as green sticks and labeled. OL and IL indicate the outer and inner leaflets of the viral membrane, respectively. C) Closeup of the spike showing the fit of the Gn^B tetramer in the cET map (for clarity, the Gc moiety in the front was removed). The cET density for the phospholipid headgroups of the outer leaflet (OL) of the viral membrane is indicated. D) Closeups of selected regions corresponding to the dashed boxes of panels A to C to show the quality of the fitting. The panels are color-framed to match the corresponding dashed boxes in the panels just above. E) Reconstruction of a Tula virus particle generated by back-projecting the 11.4 Å cET/STA density of the spike to its original location on the particle. The resulting surface protein lattice is shown in cyan with the viral membrane in gray. F-G) Ribbon representation of the spike in a top view (F) along the 4-fold axis with one of the four spike protomers colored as in Figure 1 and the sugar residues in green and in side view (G). Because the Gn^B tetramer at the spike center is occluded in this view, we omitted a large portion of the forefront Gc subunit (indicated within a dashed oval in panel F) to make it apparent.

Figure 3. The hantavirus Gn/Gc prefusion heterodimer. A) Diagrammatic representation of the single open reading frame of the hantavirus medium genomic RNA segment . The Gn signal sequence is shown in red, and other trans-membrane regions in black. "Y" symbols indicate *N*-linked glycosylation

sequons in ANDV. Gn domains A, B, and the β-ribbon are respectively colored green, blue, and pink with the remainder in white; Gc domains I, II, III, are colored red, yellow and blue, the *cd* loop in orange and the C-terminal "stem" in cyan. B) The 2.2 Å resolution structure of the MAPV Gn^H/Gc heterodimer is represented as ribbons and colored as in A, with the disulfide bonds and the *N*-glycans displayed as sticks colored according to atom type with sulfur, carbon and oxygen atoms in green, white and red, respectively. C) Orthogonal view of the Gn^H/Gc interface seen from domain II tip. The *N*-gycans and the side chains involved in inter-chain interactions are displayed as sticks and labelled. D) Ribbon representation of HNTV Gc monomer centered on domain I, showing the extended conformation adopted by Gc in the absence of the stem. Domain I is in the same orientation in panels B and D. The inner ($G_0H_0I_0B_0$), and outer ($F_0E_0D_0C_0$) sheets are indicated.

Figure 4. Interchain contacts stabilizing the hantavirus spike. A) Side view of the spike, omitting the front Gc subunit for clarity. The four protomers are depicted as ribbons and colored according to domains as indicated in Figure 3, with Gn^B in orange. The Gc-MPER, not resolved in the structure, was modeled as a helix (colored cyan) to indicate roughly its location in the lipid-head region of the membrane's outer layer (schematically indicated by a thick black line). B) Crystal structure of the Gn^B tetramer. In the left panel, the forefront protomer is depicted as ribbons and colored light orange. Disulfide bonds are indicated as green sticks and numbered. The hydrophobic residues exposed to the viral membrane are shown as sticks and labelled. The right panel shows the interactions between two protomers, with the two front protomers as ribbons and the interfacial residues highlighted. C, D, and E) Slices of the spike model normal to the 4-fold axis of the spike, as indicated in panel A, and viewed from the top. A dashed outline follows one spike protomer along the three radial sections displayed. C) Contacts in the membrane distal region. The *N*-linked glycan attached to Asn350 is shown as sticks. D) Contacts in the membrane proximal region. Shown are two *N*-linked glycans attached to Asn402 and Asn930, which fill the internal cavities of the spike. The region of the Gc stem disordered in the X-ray structure (dotted line in Figure 3B) projects into a cET density volume in close proximity of domain C of the clockwise protomer. E) The two amphipathic helices the Gn-MPER (at the Gn^B C-terminus) and the predicted Gc-MPER, which precede the TM segment, appear to form a platform supporting the spike. The approximate location of the three TM segments per protomer are indicated with a filled circle. The directionality of the helices is indicated with arrows pointing to the C-termini.

Figure 5. The conformational change of the domain II tip of Gc for TMIR formation. A) The post-fusion conformation. The left and central panels show a top (along the 3-fold axis) and a side view of the ANDV $(Gn/Gc)_3$ trimer with Gc in the characteristic post-fusion hairpin conformation displayed in surface representation and with Gn bound shown as green ribbons. One of the Gc subunits – placed

at the foreground in the side view – is colored by domains, with Tyr739, Trp766, and Phe900 at the tip of domain II displayed and labeled. For clarity, the Gn polypeptide chain in the front was omitted in the side view. N-linked glycans are shown as thick sticks. The right panel is the structure of ANDV Gc post-fusion trimer crystallized at pH 7.5 and depicted as in the central panel. The horizontal line indicates the location of the target membrane to which the hydrophobic TMIR at the domain II tip would insert. B) Ribbon representation of the tip of MAPV Gc domain II showing the organization of the *bc*, *cd*, and *ij* loops in the pre- (top panel) and post- (bottom panel) fusion conformations. Left and right panels are two orthogonal views, as indicated. Residues important for target membrane insertion surface and for forming the polar network around Glu757-Asp759 are depicted as sticks and labeled. Disulfide bonds are shown as green sticks. The *cd* loop is colored orange. In the prefusion conformation, the *bc* and *ij* loops are respectively buried by the Gn N138 glycan and the capping loop, as indicated.

Figure Supplementary 1. Sequence analysis of the glycoprotein precursor polyprotein. A) Hydrophobicity diagram and amino acid sequence conservation plot along the M segment polyprotein precursor with Gn and Gc colored as in Figure 3. The upper panel shows the posterior probability for each residue of being part of a transmembrane region as calculated by Phobius {Kall, 2004 #26}. The signal peptide region is colored red and the 3 transmembrane segments are in gray. The lower panel represents sequence conservation using scores (blue line) calculated from 64 hantavirus M segment sequences (listed in Methods) using the server Consurf {Ashkenazy, 2016 #27}. The scores were normalized so that the average for all residues is zero. The lowest scores correspond to the most conserved positions, and negative values represent positions more conserved than the average. The red line represents values that have been averaged in windows of 10 residues. As expected, the sequence of Gn^{H}, which is the most exposed region of Gn, displays mainly positive scores, i.e. lower conservation than the average, whereas for Gn^{B} and most of Gc it is the opposite. B and C) Multiple sequence alignment of Gn (panel B) and Gc (panel C) from seven representative hantaviruses. The alignment, which was truncated at the level of the Gn TM and intraviral segments, and the Gc intraviral tail, includes two New-World orthohantaviruses: Andes virus (ANDV, NP_604472.1) and Maporal virus (MAPV, YP_009362281), two Old-World orthohantaviruses: Hantaan virus (HNTV, CAA68456.1) and Puumala virus (PUUV, CAB43026.1), one mobatvirus: Laibin virus (LIBV, A0A0D5W3U2), one Loan virus: Longquan virus (LQNV, AGI62344.1), and one Thottimvirus: Thottapalayam virus (TPMV, A0A075IFP0). Strictly conserved residues and asparagines within *N*-linked glycosylation motifs are highlighted in red and green backgrounds, respectively. Disulfide bonds are indicated with a green number in the lower line. For MAPV and ANDV, the sequence of disordered segments in the crystals are framed in green (none in Gn^{H} and Gn^{B}, and around residue 1070 in Gc). Secondary structure elements are displayed

and labeled above the sequences on a background colored according to domains when experimentally determined, or in red on a gray background when predicted by Psipred, i.e. in regions not resolved in the X-ray model. The residues involved in Gn/Gc contacts and residues at the domain I / domain III / stem interface in the prefusion conformation are marked according to the key located at the upper right corner of the Figure.

Figure supplementary 2. Tula virus map. A cryo-EM grid was prepared with TULV particles and control Human papillomavirus (HPV) pseudovirus capsids on the same grid to confirm the handedness. A) A tomogram slice showing TULV (black arrow) and HPV (white arrow) in the same sample. Scale bar = 100nm. B-F) STA performed using a range of initial references shown on the left in grey to produce the reconstructions shown in blue on the right. B-D) HPV refinements. Isosurfaces are displayed as a full top view (left) and a magnified view of the pentons (right). E-F) TULV refinements. Isosurfaces are displayed as a full top view (left) and a magnified cutaway side view (right). B) Reference = EMD-5991. C) Reference = reversed hand EMD-5991. D) Reference = a spherical reference to eliminate the possibility of template bias. E) Reference = reversed hand EMD-3364. F) Reference = EMD-3364. HPV refines as expected, resulting in a map with T=7dextro arrangement of capsomers, when using the correctly handed reference and the sphere reference confirming that the handedness of the data is correct. The results of the TULV refinements match the reference displayed in E (the reversed EMD-3364) regardless of the handedness of the reference used. This confirms that the true handedness of the TULV particle is flipped relative to that reported in EMD-3364. G-I) The antigenic surfaces of Gn and Gc. G) Top view of the spike model obtained after fitting the crystal structure of PUUV-Gn into the cET map of Tula virus at 1.6 nm (PDB code 5FYN). The Gn molecules are depicted in surface representation (top panel) with the discontinuous epitopes of the neutralizing antibody (nAb) 5A2 colored in green and red, as indicated. The middle and bottom panels are cartoon representations colored from the N-terminal to the C-terminal residues using a rainbow ramp as indicated. The *N*-linked glycans are represented in sticks and the capping loop labelled. H) The same representation of panel G but using the spike model obtained after fitting the X-ray structure of ANDV-Gn/Gc into the correct hand cET map of Tula virus at 1.1 nm resolution. The Gc molecules are not shown, for clarity. I) The antigenic surface of Gc is shown in the context of the spike. As in H, the top and bottom panels are top and side views of the spike, in which Gn is depicted in ribbons and ramp colored from N- to C-terminus according to the colored bar, and Gc is shown as a white (central spike) or yellow surface (adjacent spikes), with the epitopes for nAbs 3D8, 3G1, 1C9, and Y5 colored as indicated. Note the orange and pale blue epitopes spanning across spikes.

Figure supplementary 3. Variable conformations of Gc in the heterodimer. A-C) Comparison of the X-ray structures of MAPV-Gn^H/Gc (A), ANDV-Gn^H/Gc-H953F mutant (B), and ANDV-Gn^H/Gc (C) obtained in this work. The three structures are presented using the same view upon alignment on Gn and colored as in Figure 3A. The domains are labeled and the main axes of inertia of domains I and II are drawn with the angle between them quoted, highlighting the flexion about the hinge in between them. D-E) Rigid body docking of the atomic structures of MAPV-GnGc (D), ANDV-GnGc-H953F (E) into the cET map of the Tula virus spike. The different hinge between domains I and II results in domain III partially out of cET density in (D). F) Superimposition of the structures of ANDV-GnGc (yellow), ANDV-GnGc-H953F (cyan), MAPV-GnGc (pink), and HNTV-Gc/scFv-A5 (green) on domain I to compare the different flexing about the domain II hinge. The conformation of ANDV-GnGc-H953F, which fits best the cET map (Table 2), is also very similar to that observed in the previously reported structure of HNTV-Gc/scFv-A5 (PDB:5LJY), which formed a crystallographic Gc dimer recapitulating the contacts between spikes on the viral particle {Guardado-Calvo, 2016 #13} {Bignon, 2019 #51}. G) Sequence conservation at the Gn and Gc surfaces. The conservation score, obtained from an alignment of 65 sequences (listed in Methods) using ESPript {Robert, 2014 #60} mapped at the surface of ANDV Gn^H and Gc using a color ramp from white (conserved) to dark purple (variable). The left and right panels show an "open book" representation of the interface between Gn and Gc. The interface is outlined in yellow and the conserved residues are labeled. H to J) Comparison of the conformation of the η1 loop from ANDV-Gn^H in complex with Gc (G), ANDV-Gn^H in complex with Gc-H953F (H), and MAPV-Gn^H in complex with Gc (I). Gn^H is shown as ribbons, Gc in surface representation and the glycan linked to Asn138 in sticks. Both subunits are colored according to domains as indicated in Figure 1A. The conserved Tyr325 and the ^{283}EDH^{285} motif are represented as sticks and labelled. F) Closeup showing the conformational variability of the capping loop in the superposed structures, color coded as indicated.

Figure supplementary 4. Comparison of the domain topology of the class II "companion" protein. Topology diagrams of hantavirus Gn (upper panel), alphavirus p62 (middle panel), and phlebovirus Gn (lower panel) colored according to domains: domain A (green), domain B (blue), domain C (gray), and the β-ribbon connector (magenta). The regions contacting E1 (alphavirus) and Gc (hantavirus) are indicated and labelled. The diagrams show that the topological arrangement in hantavirus Gn and alphavirus p62 is the same, in spite of the presence of various insertions (shown in white).

Figure supplementary 5. The membrane fusogenic reorganization of Gc. A) MAPV-Gc in pre-fusion conformation, crystallized at pH 8.5 in presence of Gn^H (left panel) shown next to HNTV-Gc in an extended conformation, crystallized at pH 7.5 in complex with a human antibody fragment (not shown)

(middle panel), and MAPV-Gc in post-fusion conformation, crystallized at pH 4.6 (right panel). The three panels are shown with domain I in the same orientation, and the structures ramp-colored from the N- to C-terminus as indicated. The domain-II tip in the extended (intermediate) and post-fusion conformations inserts into a target membrane, schematically represented by a line. Gn^H is represented as a gray surface in the left panel. B) Postfusion GC of MAPV (green), PUUV (blue), HTNV (yellow), and ANDV (orange) are superposed on domain I. The view was chosen to highlight the correlation between the conformation of the tip of domain II and the presence of the stem. C) Similar to panel B, the postfusion forms of Andes virus Gc in absence (orange) and presence (magenta) of Gn are superposed on domain I. Both structures are virtually identical except at the domain II tip. D) Closeup of the *cd* loop showing that Trp766, which is a key residue in the interaction with membranes, is exposed to solvent in the absence of Gn (upper panel) but is buried in the hydrophobic core of the tip β-sandwich in its presence (lower panel). E) Ribbon representation showing the reorganization the secondary structure elements of domain I during the fusogenic conformational change. Residues stabilizing the different conformations that drastically change the environment during the fusion reaction are shown as sticks. Secondary structures elements are labeled and colored as in A. The left panel shows domain-I in prefusion conformation, with β-strand A'_0 running parallel to B_0 in the inner ($G_0H_0I_0B_0$) sheet (expanding the Gc:Gc homo-dimeric interface at the inter-spike contact); β-strand K_0 from the stem interacting with C_0 to in the outer ($F_0E_0D_0C_0$) sheet, and a small α-helix formed by residues of the linker between domain I and III, plugging the distal end of the domain I β-sandwich. The middle panel shows domain I in the extended Gc conformation, showing that removal of the stem region does not alter its conformation but the location of domain-III. The right panel shows domain I in postfusion conformation, with β-strand A_0 forming part of an antiparallel β-sheet with I_0 and B_0 from a neighboring protomer. The residues that compose β-strand K_0 move with the rest of the stem closer to the tip of domain II, as shown in panel A. F) Closeup of the domain II tip, comparing the structures of MAPV Gc in presence (prefusion, top-left panel) and absence (postfusion, top-right panel) of Gn^H, and HNTV in presence (extended, bottom-left panel), and absence (postfusion, bottom-right panel) of the A5 antibody targeting the *bc* loop (PDB:5LJY). In addition to the changes in the *cd* loop, both Gn and A5 capture conformations of the *bc* loop that differ from those observed in the post-fusion form, illustrating the high malleability of this loop. It is noteworthy that the reorganization induced by Gn, but not the one induced by A5, results in the interaction between the conserved Lys744 and Asp759. In the post-fusion forms, Lys744 points outward, allowing Glu757 and Asp759 to form an acidic hydrogen bond that stabilizes the domain II tip in the post-fusion form, as described earlier {Guardado-Calvo, 2016 #13}.

MATERIALS AND METHODS

Protein expression and purification

In order to obtain a soluble Gn/Gc complex amenable to crystallize, we followed the approach used to crystallize the alphavirus p62/E1 glycoprotein heterodimer ectodomains (Li et al., 2010; Voss et al., 2010). The strategy involved making single-chain constructs spanning the ectodomains of both glycoproteins, in this case the hantavirus Gn and Gc, bypassing the TM segments in the precursor polyprotein by a soluble, flexible linker. The linker we used was 43-amino acids long in total with aa sequence GGSGLVPRGSGGGSGGGS**WSHPQFEK**GGGTGGGTLVPRGSGTGG. It contained two thrombin cleavage sites (underlined) at either end and as a strep-tag sequence (in bold) in the middle, separated by flexible GGGS or GGGT repeats. To optimize protein production and help in the purification, we cloned synthetic codon-optimized genes for expression in Drosophila cells (Genscript) into a modified pMT/BiP plasmid (Invitrogen, hereafter termed pT350), which translates the protein in frame with an enterokinase cleavage site and a double strep-tag at the C-terminal end of the Gc sequence.

The plasmids generated were used to obtain stable transfectants of Drosophila S2 cells together with the pCoPuro plasmid (ratio 1:20) for puromycin selection. The stable cell lines were selected and maintained in serum-free insect cell medium (GE Healthcare HyClone) containing 7 µg/ml puromycin. Cultures of 1 liter were grown in spinner flasks in serum-free insect cell medium (GE Healthcare HyClone) supplemented with 1% penicillin/streptomycin antibiotics to about 1 x 10^7 cells/mL, and the protein expression was induced with 4 µM $CdCl_2$. After 5 days, the S2 media supernatant was concentrated to 40 ml and supplemented with 10 µg/mL avidin and 0.1M Tris-HCl pH 8.0, centrifuged 30 minutes at 20,000 g and purified by strep-tactin affinity chromatography followed size exclusion chromatography using a Superdex 200 10/30 column (GE Healthcare) in 10 mM Tris-HCl 8.5, 150 mM NaCl, 1mM EDTA (hereafter buffer TN).

Initially, we produced a single chain containing the complete ectodomains of Gn (aa 21–484) and Gc (aa 652–1107) of Andes virus (strain Chile-9717869, NCBI code NP_604472.1). The majority of the protein obtained with this construct formed heterogeneous aggregates from which we could not obtain crystals. We therefore generated a different construct with the linker described above joining the Gn head (Gn^H, aa 21–374, Figure S1A) (Li et al., 2016; Rissanen et al., 2017) to the complete Gc ectodomain. Drosophila Schneider 2 cells stably transfected with the Gn^H/Gc construct secreted large amounts of protein, which were purified using affinity and size exclusion chromatography (SEC). The proteins behaved mostly as monomers in solution as assessed by multi-angle light scattering (MALS) (data not shown). Using the same approach, we produced Gn^H/Gc heterodimers from two hantavirus

orthologs, Maporal virus (MAPV, strain 222222 HV-97021050, NCBI code YP_009362281.1) and from Longquan virus (LQNV, strain Longquan-Ra-90, NCBI code AGI62346.1). We also introduced the H953F nutation in Gc of the Andes virus construct to destabilize its transition to the post-fusion form (as explained in the text). The aa sequence identity of the polyprotein precursor of Andes viruses with MAPV and LQNV is 85% and 40%, respectively. All constructs yielded large amount of soluble Gn^H/Gc secreted into the cell's supernatant. The LQNV construct led to the secretion of large molecular weight aggregates only, whose characterization we did not pursue.

We used the same plasmid for S2 cells expression to produce the isolated HNTV Gn^H (strain 76-118, UniprotKB code P08668.1), the complete ANDV and MAPV Gc ectodomains, ANDV Gn^B (aa. 375-484) and the isolated ANDV Gn domain C (aa 375–450). All these constructs secreted large amounts of protein that could be purified to homogeneity by affinity and size exclusion chromatography.

Crystallization and structure determination

Gn^H/Gc heterodimers: The fractions in the SEC run corresponding to the monomeric fraction of ANDV-Gn^H/Gc, ANDV-Gn^H/Gc-H953F, and MAPV-Gn^H/Gc were concentrated to 7 mg/mL using a Vivaspin centricon in 10 mM Tris-HCl 8.5, 150 mM NaCl (buffer TN). The flexible linker joining Gn^H and Gc was removed by adding 1 unit of biotinylated thrombin (Novagen) per mg of protein, and the mixture was incubated for 5 days at 4°C until the digestion was completed as judged by SDS-PAGE. These samples were used without further purification in crystallization trials at 18°C using the sitting-drop vapor diffusion method. Crystals of ANDV-Gn^H/Gc grew in the presence of 15-16% (w/v) PEG 3350, 125-400 mM potassium acetate, those of ANDV-Gn^H/Gc-H953F in 2.4M $(NH_4)_2HPO_4$, 0.1 M Tris-HCl pH 8.5, and those of MAPV-Gn^H/Gc in 0.1 M $MgCl_2$, 0.1 M Tris pH 8.5 and 17% (w/v) PEG 20000. Crystals were flash-frozen by immersion into a cryo-protectant containing the crystallization solution supplemented with 20% (v/v) glycerol, followed by rapid transfer into liquid nitrogen.

The structure of ANDV-Gn^H/Gc was solved by molecular replacement (MR) with Phaser from the suite PHENIX (Liebschner et al., 2019) using PUUV Gn^H (PDB code 5FXU) and HNTV-Gc (5IJY) as search models. The final model was built by combining real space model building in Coot (Emsley et al., 2010) with reciprocal space refinement with phenix.refine. The final model, which was validated with Molprobity (Williams et al., 2018), contains aa 23–374 of Gn and 659–1069 of Gc with two disordered regions: aa 124–126 (loop i_2D_A) and 697–702 (loop C_0D_0). The structures of ANDV-Gn^H/Gc-H953F, and MAPV-Gn^H/Gc were obtained by MR using the structure of ANDV-Gn^H/Gc as search model. The final model of ANDV-Gn^H/Gc-H953F contains aa 22–374 in Gn and 661–1092 in Gc, with a single internal break in Gc residues 1063–1076 (the N-terminal part of the stem). The structure of MAPV-

Gn^H/Gc contains aa 22–374 in Gn and 653–1083 in Gc; the N-terminal part of the stem (residues 1065–1076) was also disordered.

Gc postfusion trimers: The protein from the SEC factions corresponding to monomers of ANDV-Gc and MAPV-Gc, were concentrated to around 10 mg/mL in buffer TN and used in crystallization experiments. Crystals of MAPV-Gc appeared in an acidic condition containing 30% (v/v) PEG 400, 0.1 M $CdCl_2$, 0.1M Na-acetate pH 4.6. The structures were determined by MR using HNTV-Gc (5LJZ) as initial model, showed the characteristic post-fusion trimeric conformation of Gc around a crystallographic 3-fold axis. The final model contains aa 657–1069 without internal breaks. Crystals of proteolyzed ANDV-Gn^H/Gc were grown in a condition containing 16% (w/v) PEG 4000, 10% (v/v) 2-propanol, 0.2M $(NH_4)_2SO_4$, 0.1M Hepes pH 7.5. The final model contains aa 659–1069 and showed density for almost all the residues but three short breaks: 697–700 (loop C_0D_0), 765–766 and 775–778 (loop *cd*).

ANDV Gn^B crystals: The purified protein was concentrated to around 7 mg/mL in buffer TN and used for crystallization trials. Crystals appeared after 2-4 months at 18°C in two different conditions: 30% (v/v) MPD, 20 mM CaCl2, 0.1 M Na-acetate pH 4.6 (hereafter termed the acidic condition), and 35% (v/v) MPD, 0.2M NaCl, 0.1 M Hepes pH 7.5 (the basic condition). Crystals growing in the acidic condition belonged to orthorhombic $C222_1$ space group and diffracted to 1.9 Å resolution. The Mathews coefficient (Kantardjieff and Rupp, 2003) indicates 4 molecules in the asymmetric unit, and a self-rotation function clearly indicated the presence of a non-crystallographic 4-fold axis. Crystals grown in the basic condition belonged to the tetragonal space group I4 with two molecules in the asymmetric and diffracted to 2.4 Å resolution. We used experimental phasing with sodium iodide to determine their structure, as we found no good search model for MR. We soaked crystals for 20 minutes in mother liquor supplemented with 500 mM NaI before plunging them directly into liquid nitrogen. In order to optimize the anomalous signal we collected a highly redundant dataset merging three independent datasets collected from two different crystals using a kappa goniometer. The final SAD dataset showed anomalous signal up to 3.6 Å. Substructure determination and phasing were carried out using the SHELX suite (Sheldrick, 2010) and an initial model was build using phenix AutoBuild (Terwilliger et al., 2008). The final model was obtained by combining real space model building in Coot with reciprocal space refinement using phenix.refine and contains aa 379–483 with no Ramachandran outliers. Surprisingly, we found clear density between protomers in the tetramer that could be assigned a short RNA oligonucleotide (3 pyrimidine nucleotides). We used this model to solved the structure of the crystals grown at acidic pH by molecular replacement. The structure showed 4 molecules in the asymmetric unit forming a tetramer virtually identical to that observed at basic pH, including the presence of the RNA oligo between protomers.

Crystals of HTNV Gn^H at neutral pH. The available structures of HNTV Gn^H are at acidic pH. We determined its structure at neutral pH by concentrating it in TN buffer and made crystallization experiments at 18°C. We obtained crystals diffracting to 1.9 Å growing at pH 7.5 in a condition containing 25% (w/v) PEG 6000, 0.1M LiCl, 0.1M Hepes pH 7.5, and 20% (v/v) glycerol. We determined the structure using PUUV Gn^H (5FXU) as search model. The resulting HTNV Gn^H structure resolved aa 20–373 with a single internal break in the loop η1 (aa 281–290).

The X-ray diffraction data reported in this manuscript were recorded at beamlines Proxima I and II at the Synchrotron Soleil (St. Aubin, France). The statistics of all the crystals and refinement are provided in Table 1.

Conservation analysis

The conservation scores per residue showed in Figures S1 and S3 were obtained by using the program Espript (Robert and Gouet, 2014) and a multiple sequence alignment generated by Clustal omega (Sievers et al., 2011) using a set of 69 hantaviral sequences extracted from (Zhang et al., 2013). The GenBank accession numbers for the sequences used in the analysis are: JX465398, JX465397, JX465402, JX465399, JX465400, JX465401, JF784178, NC_010708, EF641799, EF641806, HQ834696, FJ539167, EU929073, EU929074, HM015219, EF543526, JX465390, JX465391, JX465392, JX465393, JX465394, JX465395, JX465403, Y00386, AF143675, AB620029, AY675353, AB027115, GF796031, AY168577, AJ410616, GQ205412, AY961616, JQ082301, AF288298, GU592827, EF990916, L08756, GQ274938, HM756287, AB297666, AB433850, EF198413, AJ011648, EU072489, AJ011647, EU072488, Z69993, X55129, L36930, DQ177347, L39950, DQ284451, DQ285047, AB620104, AB620107, U26828, AB620101, U36801, U36802, AF030551, L33474, L37903, AF291703, AF028024, AF005728, FJ608550, AY363179, AF307323.

VLP expression and design of Gn/Gc mutants

For ANDV VLP expression we used the plasmid pI.18/GPC that encodes the full length glycoprotein precursor of ANDV strain CHI-7913 under the control of the cytomegalovirus promotor (termed pI.18/GPC) (Cifuentes-Munoz et al., 2011). Site-directed mutagenesis was done by DNA synthesis and sub-cloning into pI.18/GPC using intrinsic restriction sites (GenScript). Briefly, 293FT cells (Thermo Fisher Scientific) maintained in DMEM supplemented with 10% FCS were grown in 100 mm plates and calcium-transfected with the pI.18/GPC wild type or the different mutant constructs. 48 h later the cell surface proteins were labeled with biotin in order to separate the biotinylated (surface proteins) from non-biotinylated (intracellular proteins) fractions using a cell surface protein isolation kit (Pierce). For protein detection by western blot, primary anti-Gc monoclonal antibodies 2H4/F6 and 5D11/G7 (Cifuentes-Munoz et al., 2011; Godoy et al., 2009), anti-Gn monoclonal antibody 6B9/F5

(Cifuentes-Munoz et al., 2011) or anti-β-actin MAb (Sigma) were used at 1:2.500 and subsequently detected with an anti-mouse immunoglobulin horseradish peroxidase conjugate (Thermo Fisher Scientific) 1:5.000 and a chemiluminescent substrate (Pierce). All these antibodies were previously characterized (Cifuentes-Munoz et al., 2011). For Gn/Gc VLP production, the supernatant of transfected 293FT cells were harvested at 48 h post-transfection and concentrated as previously established (Acuna et al., 2015).

Tula virus growth and purification

Tula virus (TULV, strain Moravia) was cultivated on Vero E6 cells (ATCC 94 CRL-1586), as previously described (Huiskonen et al., 2010). Four days post infection (dpi), the growth medium (DMEM, Sigma) was replaced by medium supplemented with 3% fetal calf serum (FCS). At 5, 6 and 7 dpi the virus-containing medium was collected and clarified by centrifugation (3,000 × g for 30 min) to remove large cell debris. The medium was then concentrated 100-fold using a 100-kDa cut-off filter (Amicon) and placed on top of a 25–65% sucrose density gradient (in standard buffer [20 mM Tris and 100 mM NaCl pH 7.0]) in a SW32.1 tube (Beckman Coulter), and the virus was banded by ultracentrifugation (SW32 Ti rotor, 25,000 rpm, 4°C, 12 h). Virus-containing fractions were pooled and diluted 1:1 in 20 mM Tris and 100 mM NaCl before pelleting by ultracentrifugation (Beckman Coulter TLS 55 rotor, 50,000 rpm, 4°C, 2 h). The virus pellet was resuspended in the standard buffer.

An aliquot (3µl) of each sample was applied to 1.2-µm hole carbon grids (C-flat, Protochips) that were then floated on a droplet of standard buffer to remove residual sucrose. An aliquot (3 µl) of 6-nm gold fiducial markers was added to enable tilt series alignment. The sample was then vitrified by plunge freezing to liquid ethane-propane mixture by using a vitrification apparatus (CP3, Leica).

EM Data Acquisition

Data were collected using a Tecnai F30 “Polara” transmission electron microscope (FEI) operated at 300 kV and at liquid nitrogen temperature. SerialEM (Mastronarde, 2005) was used to acquire images on a direct electron detector (K2 Summit; Gatan) mounted behind an energy filter (QIF Quantum LS; Gatan). A total of 49 tilt series were collected from –30 to 60 degrees in 3 degree increments with a dose of 4.71 $e^{-}/Å^{2}$ per tilt. For each tilt image 6 movie frames were acquired at a calibrated magnification of ×25,000, corresponding to a pixel size of 2 Å. Defocus was varied from 2.5 µm to 4.0 µm between the tilt series.

Cryo-EM Data Processing

Movie frames were aligned and averaged using motioncor2 to correct for beam induced motion (Zheng et al., 2017). Contrast transfer function (CTF) parameters were estimated using

CTFFIND4 (Rohou and Grigorieff, 2015) and a dose-weighting filter was applied to the images according to their accumulated electron dose as described previously (Grant and Grigorieff, 2015). These pre-processing steps were carried out using a custom set of scripts named “tomo_preprocess” (available upon request). Tilt images were then aligned using gold fiducial markers in IMOD (Kremer et al., 1996), corrected for the effect of CTF by phase flipping and used to reconstruct the tomograms by weighted back projection in IMOD (Mastronarde and Held, 2017). Subtomogram averaging was performed in Dynamo (Castano-Diez et al., 2012). Initial particles for this refinement were created by modelling the surface of the membrane using the Dynamo’s tomoview function and defining their initial orientation normal to this surface. These initial ‘seeds’ were more densely populated than the true spikes and overlapping spikes were removed based on cross-correlation after each iteration in the refinement. Refinements were carried out with C4 symmetry using the existing Tula virus spike map as a reference (EMD-3364). The map was low-pass filtered to 50 Å resolution to avoid model bias. A custom script “patch_finder” (available upon request) was used to restrict the dataset to only those particles that formed regular patches on the surface of the virions. The final dataset was subjected to 3D classification in RELION (Bharat and Scheres, 2016) before further refinement in Dynamo. The amplitudes of the final maps were weighted to correct for the effect of dose-weighting of the original images using a custom script (available on request). The final reconstruction, comprised of ~18,064 subvolumes, was filtered to 11.4 Å as determined by FSC (0.143 threshold). The threshold value for the rendered isosurface was determined according to the molecular weight of the viral ectodomain proteins assuming an average protein density of 0.81 Da/Å^3.

Handedness testing

Grids were prepared as previously described with Tula premixed with a sample of recombinantly produced human papillomavirus (HPV) type 16 pseudovirus capsids (a kind gift from Dr. Kay Grünewald). A total of 7 tilt series were collected from –45 to 45 degrees in 5 degree increments with a dose of 5.5 e^-/Å^2 per tilt. For each tilt image, 8 movie frames were acquired at a calibrated magnification of ×37,037, corresponding to a pixel size of 1.35 Å. Defocus was varied from 3 µm to 4 µm between the tilt series. Tomograms were reconstructed as described above. Subtomogram averaging of both TULV spikes and HPV particles were performed in Dynamo following the same workflow. Icosahedral symmetry was assumed for HPV averaging using reference EMD-5991 and C4 symmetry was assumed for TULV averaging using reference EMD-3364. Multiple refinements were carried out with references of each hand to eliminate the possibility of template bias.

REFERENCES

Acuna, R., Bignon, E.A., Mancini, R., Lozach, P.Y., and Tischler, N.D. (2015). Acidification triggers Andes hantavirus membrane fusion and rearrangement of Gc into a stable post-fusion homotrimer. J Gen Virol *96*, 3192-3197.
Antic, D., Wright, K.E., and Kang, C.Y. (1992). Maturation of Hantaan virus glycoproteins G1 and G2. Virology *189*, 324-328.
Battisti, A.J., Chu, Y.K., Chipman, P.R., Kaufmann, B., Jonsson, C.B., and Rossmann, M.G. (2011). Structural studies of Hantaan virus. J Virol *85*, 835-841.
Bharat, T.A., and Scheres, S.H. (2016). Resolving macromolecular structures from electron cryo-tomography data using subtomogram averaging in RELION. Nat Protoc *11*, 2054-2065.
Bignon, E.A., Albornoz, A., Guardado-Calvo, P., Rey, F.A., and Tischler, N.D. (2019). Molecular organization and dynamics of the fusion protein Gc at the hantavirus surface. Elife *8*.
Bressanelli, S., Stiasny, K., Allison, S.L., Stura, E.A., Duquerroy, S., Lescar, J., Heinz, F.X., and Rey, F.A. (2004). Structure of a flavivirus envelope glycoprotein in its low-pH-induced membrane fusion conformation. EMBO J *23*, 728-738.
Buchan, D.W.A., and Jones, D.T. (2019). The PSIPRED Protein Analysis Workbench: 20 years on. Nucleic Acids Res *47*, W402-W407.
Castano-Diez, D., Kudryashev, M., Arheit, M., and Stahlberg, H. (2012). Dynamo: a flexible, user-friendly development tool for subtomogram averaging of cryo-EM data in high-performance computing environments. J Struct Biol *178*, 139-151.
Chiang, C.F., Flint, M., Lin, J.S., and Spiropoulou, C.F. (2016). Endocytic Pathways Used by Andes Virus to Enter Primary Human Lung Endothelial Cells. PLoS One *11*, e0164768.
Cifuentes-Munoz, N., Barriga, G.P., Valenzuela, P.D., and Tischler, N.D. (2011). Aromatic and polar residues spanning the candidate fusion peptide of the Andes virus Gc protein are essential for membrane fusion and infection. J Gen Virol *92*, 552-563.
Cifuentes-Munoz, N., Salazar-Quiroz, N., and Tischler, N.D. (2014). Hantavirus Gn and Gc envelope glycoproteins: key structural units for virus cell entry and virus assembly. Viruses *6*, 1801-1822.
Cooper, R.S., Georgieva, E.R., Borbat, P.P., Freed, J.H., and Heldwein, E.E. (2018). Structural basis for membrane anchoring and fusion regulation of the herpes simplex virus fusogen gB. Nat Struct Mol Biol *25*, 416-424.
Craig, D.B., and Dombkowski, A.A. (2013). Disulfide by Design 2.0: a web-based tool for disulfide engineering in proteins. BMC Bioinformatics *14*, 346.
Dessau, M., and Modis, Y. (2013). Crystal structure of glycoprotein C from Rift Valley fever virus. Proc Natl Acad Sci U S A *110*, 1696-1701.
Emsley, P., Lohkamp, B., Scott, W.G., and Cowtan, K. (2010). Features and development of Coot. Acta Crystallogr D Biol Crystallogr *66*, 486-501.
Fedry, J., Liu, Y., Pehau-Arnaudet, G., Pei, J., Li, W., Tortorici, M.A., Traincard, F., Meola, A., Bricogne, G., Grishin, N.V.*, et al.* (2017). The Ancient Gamete Fusogen HAP2 Is a Eukaryotic Class II Fusion Protein. Cell *168*, 904-915 e910.
Fu, Q., Shaik, M.M., Cai, Y., Ghantous, F., Piai, A., Peng, H., Rits-Volloch, S., Liu, Z., Harrison, S.C., Seaman, M.S.*, et al.* (2018). Structure of the membrane proximal external region of HIV-1 envelope glycoprotein. Proc Natl Acad Sci U S A *115*, E8892-E8899.
Gibbons, D.L., Vaney, M.C., Roussel, A., Vigouroux, A., Reilly, B., Lepault, J., Kielian, M., and Rey, F.A. (2004). Conformational change and protein-protein interactions of the fusion protein of Semliki Forest virus. Nature *427*, 320-325.

Godoy, P., Marsac, D., Stefas, E., Ferrer, P., Tischler, N.D., Pino, K., Ramdohr, P., Vial, P., Valenzuela, P.D., Ferres, M.*, et al.* (2009). Andes virus antigens are shed in urine of patients with acute hantavirus cardiopulmonary syndrome. J Virol *83*, 5046-5055.
Grant, T., and Grigorieff, N. (2015). Measuring the optimal exposure for single particle cryo-EM using a 2.6 A reconstruction of rotavirus VP6. Elife *4*, e06980.
Guardado-Calvo, P., Atkovska, K., Jeffers, S.A., Grau, N., Backovic, M., Perez-Vargas, J., de Boer, S.M., Tortorici, M.A., Pehau-Arnaudet, G., Lepault, J.*, et al.* (2017). A glycerophospholipid-specific pocket in the RVFV class II fusion protein drives target membrane insertion. Science *358*, 663-667.
Guardado-Calvo, P., Bignon, E.A., Stettner, E., Jeffers, S.A., Perez-Vargas, J., Pehau-Arnaudet, G., Tortorici, M.A., Jestin, J.L., England, P., Tischler, N.D.*, et al.* (2016). Mechanistic Insight into Bunyavirus-Induced Membrane Fusion from Structure-Function Analyses of the Hantavirus Envelope Glycoprotein Gc. PLoS Pathog *12*, e1005813.
Guardado-Calvo, P., and Rey, F.A. (2017). The Envelope Proteins of the Bunyavirales. Adv Virus Res *98*, 83-118.
Halldorsson, S., Li, S., Li, M., Harlos, K., Bowden, T.A., and Huiskonen, J.T. (2018). Shielding and activation of a viral membrane fusion protein. Nat Commun *9*, 349.
Heiskanen, T., Lundkvist, A., Soliymani, R., Koivunen, E., Vaheri, A., and Lankinen, H. (1999). Phage-displayed peptides mimicking the discontinuous neutralization sites of puumala Hantavirus envelope glycoproteins. Virology *262*, 321-332.
Hepojoki, J., Strandin, T., Vaheri, A., and Lankinen, H. (2010). Interactions and oligomerization of hantavirus glycoproteins. J Virol *84*, 227-242.
Huiskonen, J.T., Hepojoki, J., Laurinmaki, P., Vaheri, A., Lankinen, H., Butcher, S.J., and Grunewald, K. (2010). Electron cryotomography of Tula hantavirus suggests a unique assembly paradigm for enveloped viruses. J Virol *84*, 4889-4897.
Jangra, R.K., Herbert, A.S., Li, R., Jae, L.T., Kleinfelter, L.M., Slough, M.M., Barker, S.L., Guardado-Calvo, P., Roman-Sosa, G., Dieterle, M.E.*, et al.* (2018). Protocadherin-1 is essential for cell entry by New World hantaviruses. Nature *563*, 559-563.
Jin, M., Park, J., Lee, S., Park, B., Shin, J., Song, K.J., Ahn, T.I., Hwang, S.Y., Ahn, B.Y., and Ahn, K. (2002). Hantaan virus enters cells by clathrin-dependent receptor-mediated endocytosis. Virology *294*, 60-69.
Jonsson, C.B., Figueiredo, L.T., and Vapalahti, O. (2010). A global perspective on hantavirus ecology, epidemiology, and disease. Clin Microbiol Rev *23*, 412-441.
Kantardjieff, K.A., and Rupp, B. (2003). Matthews coefficient probabilities: Improved estimates for unit cell contents of proteins, DNA, and protein-nucleic acid complex crystals. Protein Sci *12*, 1865-1871.
Koch, J., Liang, M., Queitsch, I., Kraus, A.A., and Bautz, E.K. (2003). Human recombinant neutralizing antibodies against hantaan virus G2 protein. Virology *308*, 64-73.
Krarup, A., Truan, D., Furmanova-Hollenstein, P., Bogaert, L., Bouchier, P., Bisschop, I.J.M., Widjojoatmodjo, M.N., Zahn, R., Schuitemaker, H., McLellan, J.S.*, et al.* (2015). A highly stable prefusion RSV F vaccine derived from structural analysis of the fusion mechanism. Nat Commun *6*, 8143.
Kremer, J.R., Mastronarde, D.N., and McIntosh, J.R. (1996). Computer visualization of three-dimensional image data using IMOD. J Struct Biol *116*, 71-76.
Lescar, J., Roussel, A., Wien, M.W., Navaza, J., Fuller, S.D., Wengler, G., Wengler, G., and Rey, F.A. (2001). The Fusion glycoprotein shell of Semliki Forest virus: an icosahedral assembly primed for fusogenic activation at endosomal pH. Cell *105*, 137-148.

Li, L., Jose, J., Xiang, Y., Kuhn, R.J., and Rossmann, M.G. (2010). Structural changes of envelope proteins during alphavirus fusion. Nature *468*, 705-708.
Li, L., Lok, S.M., Yu, I.M., Zhang, Y., Kuhn, R.J., Chen, J., and Rossmann, M.G. (2008). The flavivirus precursor membrane-envelope protein complex: structure and maturation. Science *319*, 1830-1834.
Li, S., Rissanen, I., Zeltina, A., Hepojoki, J., Raghwani, J., Harlos, K., Pybus, O.G., Huiskonen, J.T., and Bowden, T.A. (2016). A Molecular-Level Account of the Antigenic Hantaviral Surface. Cell Rep *15*, 959-967.
Liebschner, D., Afonine, P.V., Baker, M.L., Bunkoczi, G., Chen, V.B., Croll, T.I., Hintze, B., Hung, L.W., Jain, S., McCoy, A.J.*, et al.* (2019). Macromolecular structure determination using X-rays, neutrons and electrons: recent developments in Phenix. Acta Crystallogr D Struct Biol *75*, 861-877.
Lober, C., Anheier, B., Lindow, S., Klenk, H.D., and Feldmann, H. (2001). The Hantaan virus glycoprotein precursor is cleaved at the conserved pentapeptide WAASA. Virology *289*, 224-229.
Luca, V.C., Nelson, C.A., and Fremont, D.H. (2013). Structure of the St. Louis encephalitis virus postfusion envelope trimer. J Virol *87*, 818-828.
Lundkvist, A., and Niklasson, B. (1992). Bank vole monoclonal antibodies against Puumala virus envelope glycoproteins: identification of epitopes involved in neutralization. Arch Virol *126*, 93-105.
Maes, P., Adkins, S., Alkhovsky, S.V., Avsic-Zupanc, T., Ballinger, M.J., Bente, D.A., Beer, M., Bergeron, E., Blair, C.D., Briese, T.*, et al.* (2019). Taxonomy of the order Bunyavirales: second update 2018. Arch Virol *164*, 927-941.
Martin, M.L., Lindsey-Regnery, H., Sasso, D.R., McCormick, J.B., and Palmer, E. (1985). Distinction between Bunyaviridae genera by surface structure and comparison with Hantaan virus using negative stain electron microscopy. Arch Virol *86*, 17-28.
Martinez, V.P., Bellomo, C., San Juan, J., Pinna, D., Forlenza, R., Elder, M., and Padula, P.J. (2005). Person-to-person transmission of Andes virus. Emerg Infect Dis *11*, 1848-1853.
Martyna, A., Bahsoun, B., Badham, M.D., Srinivasan, S., Howard, M.J., and Rossman, J.S. (2017). Membrane remodeling by the M2 amphipathic helix drives influenza virus membrane scission. Sci Rep *7*, 44695.
Mastronarde, D.N. (2005). Automated electron microscope tomography using robust prediction of specimen movements. J Struct Biol *152*, 36-51.
Mastronarde, D.N., and Held, S.R. (2017). Automated tilt series alignment and tomographic reconstruction in IMOD. J Struct Biol *197*, 102-113.
Mittler, E., Dieterle, M.E., Kleinfelter, L.M., Slough, M.M., Chandran, K., and Jangra, R.K. (2019). Hantavirus entry: Perspectives and recent advances. Adv Virus Res *104*, 185-224.
Modis, Y. (2014). Relating structure to evolution in class II viral membrane fusion proteins. Curr Opin Virol *5*, 34-41.
Modis, Y., Ogata, S., Clements, D., and Harrison, S.C. (2004). Structure of the dengue virus envelope protein after membrane fusion. Nature *427*, 313-319.
Padula, P.J., Edelstein, A., Miguel, S.D., Lopez, N.M., Rossi, C.M., and Rabinovich, R.D. (1998). Hantavirus pulmonary syndrome outbreak in Argentina: molecular evidence for person-to-person transmission of Andes virus. Virology *241*, 323-330.
Pallesen, J., Wang, N., Corbett, K.S., Wrapp, D., Kirchdoerfer, R.N., Turner, H.L., Cottrell, C.A., Becker, M.M., Wang, L., Shi, W.*, et al.* (2017). Immunogenicity and structures of a rationally designed prefusion MERS-CoV spike antigen. Proc Natl Acad Sci U S A *114*, E7348-E7357.

Perez-Vargas, J., Krey, T., Valansi, C., Avinoam, O., Haouz, A., Jamin, M., Raveh-Barak, H., Podbilewicz, B., and Rey, F.A. (2014). Structural basis of eukaryotic cell-cell fusion. Cell *157*, 407-419.
Pettersen, E.F., Goddard, T.D., Huang, C.C., Couch, G.S., Greenblatt, D.M., Meng, E.C., and Ferrin, T.E. (2004). UCSF Chimera--a visualization system for exploratory research and analysis. J Comput Chem *25*, 1605-1612.
Pizarro, E., Navarrete, M., Mendez, C., Zaror, L., Mansilla, C., Tapia, M., Carrasco, C., Salazar, P., Murua, R., Padula, P.*, et al.* (2019). Immunocytochemical and Ultrastructural Evidence Supporting That Andes Hantavirus (ANDV) Is Transmitted Person-to-Person Through the Respiratory and/or Salivary Pathways. Front Microbiol *10*, 2992.
Ramanathan, H.N., and Jonsson, C.B. (2008). New and Old World hantaviruses differentially utilize host cytoskeletal components during their life cycles. Virology *374*, 138-150.
Rey, F.A., Heinz, F.X., Mandl, C., Kunz, C., and Harrison, S.C. (1995). The envelope glycoprotein from tick-borne encephalitis virus at 2 A resolution. Nature *375*, 291-298.
Rissanen, I., Stass, R., Zeltina, A., Li, S., Hepojoki, J., Harlos, K., Gilbert, R.J.C., Huiskonen, J.T., and Bowden, T.A. (2017). Structural Transitions of the Conserved and Metastable Hantaviral Glycoprotein Envelope. J Virol *91*.
Robert, X., and Gouet, P. (2014). Deciphering key features in protein structures with the new ENDscript server. Nucleic Acids Res *42*, W320-324.
Rohou, A., and Grigorieff, N. (2015). CTFFIND4: Fast and accurate defocus estimation from electron micrographs. J Struct Biol *192*, 216-221.
Rutten, L., Gilman, M.S.A., Blokland, S., Juraszek, J., McLellan, J.S., and Langedijk, J.P.M. (2020). Structure-Based Design of Prefusion-Stabilized Filovirus Glycoprotein Trimers. Cell Rep *30*, 4540-4550 e4543.
Schmaljohn, C.S., Hasty, S.E., Rasmussen, L., and Dalrymple, J.M. (1986). Hantaan virus replication: effects of monensin, tunicamycin and endoglycosidases on the structural glycoproteins. J Gen Virol *67 (Pt 4)*, 707-717.
Sheldrick, G.M. (2010). Experimental phasing with SHELXC/D/E: combining chain tracing with density modification. Acta Crystallogr D Biol Crystallogr *66*, 479-485.
Shi, X., and Elliott, R.M. (2004). Analysis of N-linked glycosylation of hantaan virus glycoproteins and the role of oligosaccharide side chains in protein folding and intracellular trafficking. J Virol *78*, 5414-5422.
Sievers, F., Wilm, A., Dineen, D., Gibson, T.J., Karplus, K., Li, W., Lopez, R., McWilliam, H., Remmert, M., Soding, J.*, et al.* (2011). Fast, scalable generation of high-quality protein multiple sequence alignments using Clustal Omega. Mol Syst Biol *7*, 539.
Slough, M.M., Chandran, K., and Jangra, R.K. (2019). Two Point Mutations in Old World Hantavirus Glycoproteins Afford the Generation of Highly Infectious Recombinant Vesicular Stomatitis Virus Vectors. MBio *10*.
Terwilliger, T.C., Grosse-Kunstleve, R.W., Afonine, P.V., Moriarty, N.W., Zwart, P.H., Hung, L.W., Read, R.J., and Adams, P.D. (2008). Iterative model building, structure refinement and density modification with the PHENIX AutoBuild wizard. Acta Crystallogr D Biol Crystallogr *64*, 61-69.
Voss, J.E., Vaney, M.C., Duquerroy, S., Vonrhein, C., Girard-Blanc, C., Crublet, E., Thompson, A., Bricogne, G., and Rey, F.A. (2010). Glycoprotein organization of Chikungunya virus particles revealed by X-ray crystallography. Nature *468*, 709-712.
Watanabe, Y., Bowden, T.A., Wilson, I.A., and Crispin, M. (2019). Exploitation of glycosylation in enveloped virus pathobiology. Biochim Biophys Acta Gen Subj *1863*, 1480-1497.

Willensky, S., Bar-Rogovsky, H., Bignon, E.A., Tischler, N.D., Modis, Y., and Dessau, M. (2016). Crystal Structure of Glycoprotein C from a Hantavirus in the Post-fusion Conformation. PLoS Pathog *12*, e1005948.
Williams, C.J., Headd, J.J., Moriarty, N.W., Prisant, M.G., Videau, L.L., Deis, L.N., Verma, V., Keedy, D.A., Hintze, B.J., Chen, V.B.*, et al.* (2018). MolProbity: More and better reference data for improved all-atom structure validation. Protein Sci *27*, 293-315.
Xu, Z., Wei, L., Wang, L., Wang, H., and Jiang, S. (2002). The in vitro and in vivo protective activity of monoclonal antibodies directed against Hantaan virus: potential application for immunotherapy and passive immunization. Biochem Biophys Res Commun *298*, 552-558.
Zhang, X., Ge, P., Yu, X., Brannan, J.M., Bi, G., Zhang, Q., Schein, S., and Zhou, Z.H. (2013). Cryo-EM structure of the mature dengue virus at 3.5-A resolution. Nat Struct Mol Biol *20*, 105-110.
Zhang, Y., Zhang, W., Ogata, S., Clements, D., Strauss, J.H., Baker, T.S., Kuhn, R.J., and Rossmann, M.G. (2004). Conformational changes of the flavivirus E glycoprotein. Structure *12*, 1607-1618.
Zheng, S.Q., Palovcak, E., Armache, J.P., Verba, K.A., Cheng, Y., and Agard, D.A. (2017). MotionCor2: anisotropic correction of beam-induced motion for improved cryo-electron microscopy. Nat Methods *14*, 331-332.

Table 1. Crystallographic statistics								
	ANDV-Gn^{H}Gc	**ANDV-Gn^{H}Gc (H953F)**	**MAPV-Gn^{H}Gc**	**ANDV-Gc pH 7.5**	**MAPV-Gc pH 4.6**	**HNTV-Gn^{H} pH 7.5**	**Gn^{B} pH 4.6**	**Gn^{B} pH 7.5**
Data collection								
Space group	H 3	P 6_3 2 2	C 1 2 1	H 32	H 32	P 2_1 2_1 2_1	C 2 2 2_1	I 4
a (Å)	130.3	188.5	120.3	92.6	90.4	53.6	90.6	67.8
b (Å)	130.3	188.5	65.1	92.6	90.4	92.2	123.1	67.8
c (Å)	129.5	117.3	144.9	318.5	506.4	94.0	90.1	121.9
β (°)	90	90	99.7	90	90	90	90	90
Resolution (Å)	37.62-2.55	49.36-3.20	38.07-2.20	39.80-2.70	39.83-2.40	35.34-1.94	45.3-1.90	37.7-2.35
Last resolution bin (Å)	2.66-2.55	3.42-3.20	2.26-2.20	2.83-2.70	2.49-2.40	1.98-1.94	1.94-1.90	2.43-2.35
Total observations	68478 (8692)	335389 (59067)	258945 (13723)	139957 (18675)	482431 (52803)	289204 (18180)	542782(31473)	114803 (10501)
Unique reflections	25995 (3241)	20744 (3657)	55909 (4505)	14898 (1949)	31958 (3310)	35256 (2248)	39873 (2451)	11445 (1080)
Completeness (%)	97.3 (99.8)	99.8 (99.4)	99.5 (98.9)	99.8 (99.9)	100 (100)	99.6 (95.6)	99.8(97.0)	99.6(96.4)
Redundancy	2.6 (2.7)	16.2 (16.2)	4.6 (3.0)	9.4 (9.6)	15.1 (16.0)	8.2 (8.1)	13.6(12.8)	10.0(9.7)
<I/σ>	11.2 (1.4)	13.5 (1.2)	11.0 (0.9)	8.2 (1.2)	11.1 (1.0)	14.6 (1.8)	11.1(0.9)	8.1(1.7)
Rsym (%)	5.7 (73.5)	19.2 (269.5)	8.2 (114.1)	13.6 (120)	16.9 (262)	7.6 (105)	11.2(288)	18.4(121)
$CC_{1/2}$	99.7 (49.0)	99.9 (53.2)	99.7 (33.8)	99.7 (91.8)	99.8 (50.6)	99.9 (65.5)	99.8(53.7)	98.8(45.5)
Refinement								
PDB accesion code	6Y5W	6Y5F	6Y62	6Y6Q	6Y68	6Y6P	6YRQ	6YRB
Resolution (Å)	37.62-2.55	49.63-3.20	35.14-2.20	39.80-2.70	39.83-2.40	35.35-1.94	45.3-1.90	37.7-2.35
Last resolution bin (Å)	2.64-2.55	3.36-3.20	2.24-2.20	2.79-2.70	2.44-2.40	1.99-1.94	1.94-1.90	2.58-2.35
Nb.of reflections	25987 (2465)	20680 (2685)	55841 (2606)	14734 (2625)	31948 (2798)	35189 (2661)	39739 (2560)	11444 (2691)
Nb.of reflections for Rfree	1360 (165)	1032 (157)	2814 (132)	1338 (122)	2914 (128)	1673 (153)	1957(123)	570(126)
Rfactor (%)	21.8 (33.0)	21.4 (34.2)	19.4 (31.4)	23.4 (37.7)	19.6 (32.2)	16.7 (23.0)	18.7(38.2)	22.6(29.8)
Rfree (%)	26.1 (35.7)	26.6 (44.9)	22.6 (35.8)	28.7 (34.2)	23.6 (33.6)	21.0 (25.2)	23.0(42.2)	26.5(34.2)
Nb. of protein+sugar atoms (chain A/B/C/D)	2776/3144	2809 / 3201	2801/3208	3084	3204	2745	767/744/ 772/806	803/744
Nb. of waters/Cd^{+2}/I^{-}	64	1	261	4	83/4	202	137	55/0/6
Nb. of $(PO_4)^{-2}$/$(SO_4)^{-2}$ atoms		10/0		0/10				
Nb. of RNA/MPD atoms							256/32	130
Mean B value (Å^2)								
Protein+sugar (A/B/C/D)	85.6/57.1	104.8 / 104.0	52.3/63.9	98.0	70.2	46.5	52/54/53/55	46/48
Waters/ Cd^{+2}/I^{-}	50.0	78.6	49.4	66	57.0/125	47.6	52	43/-/115
$(PO4)^{-2}$/$(SO_4)^{-2}$ atoms		161		0/152				
RNA/MPD							53/67	52
Root mean square deviations								
Bond lengths (Å)	0.002	0.007	0.006	0.003	0.008	0.018	0.006	0.002
Bond angles (°)	0.56	1.111	0.707	0.600	0.935	1.419	0.923	0.546
Ramachandran favored/outliers (%)	93.6/0.0	91.7/0.5	95.0/0.0	94.3/0.26	95.4/0.5	94.7/0.3	97.1/0.0	97.38/0.0

Table 2. EM fitting statistics				
	Unconstrained fitting[1]		Constrained fitting[2]	
	CC	% atoms inside	CC	% atoms inside
ANDV-H953F Gn/Gc				
Central	0.888	88.9	0.861	82.8
Neighbour	0.880	80.0	0.834	69.9
Dimer	0.884	84.5	0.857	76.3
MAPV Gn/Gc				
Central	0.873	84.6	0.812	74.8
Neighbour	0.867	76.5	0.814	63.9
Dimer	0.870	80.6	0.816	69.4
ANDV Domain C				
Central			0.882	87.1

1. Fitting a protomer of ANDV-H953F Gn/Gc or MAPV Gn/Gc
2. Fitting a dimer of ANDV-H953F Gn/Gc or MAPV Gn/Gc and a tetramer of ANDV Domain C

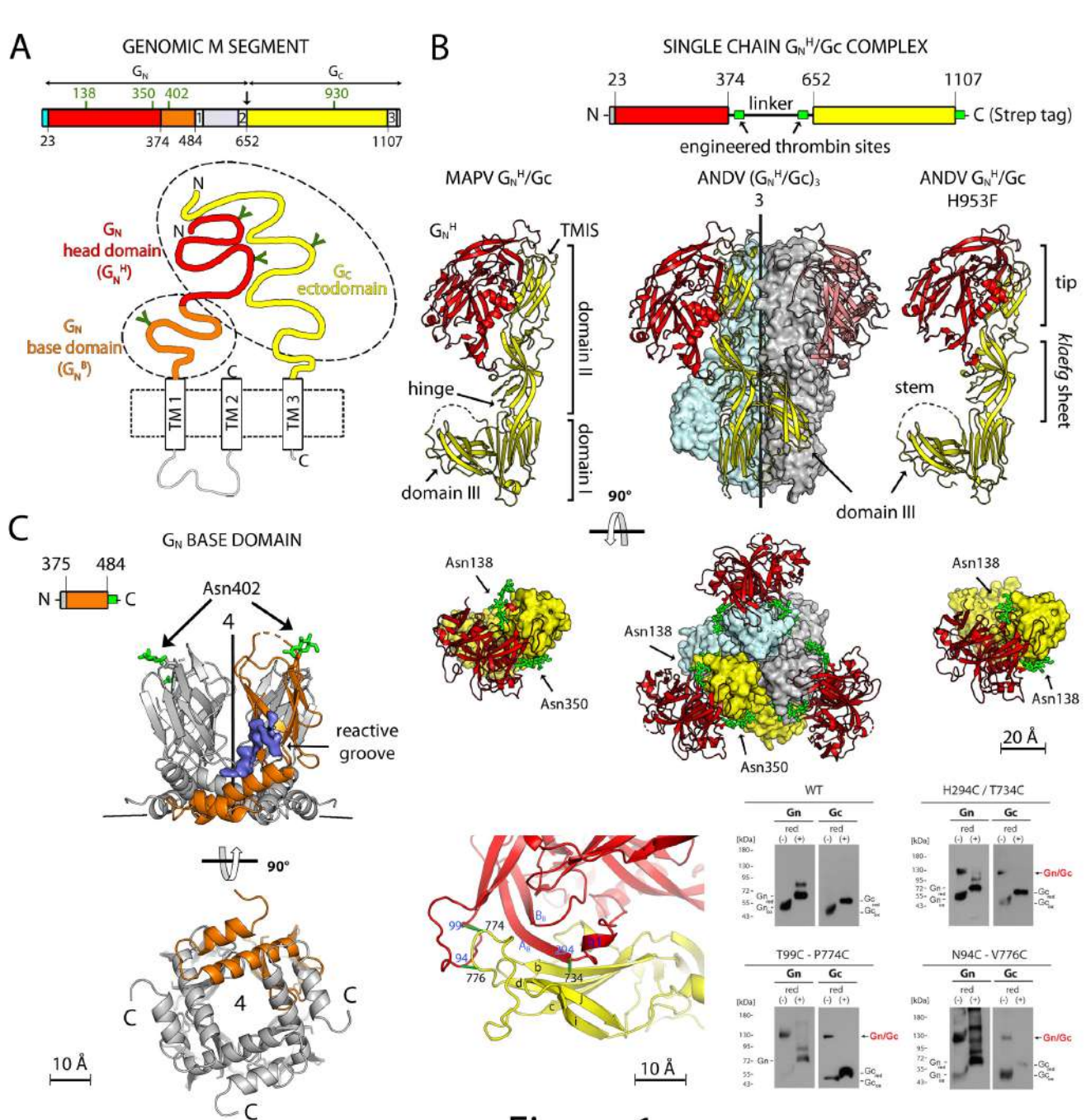

Figure 1

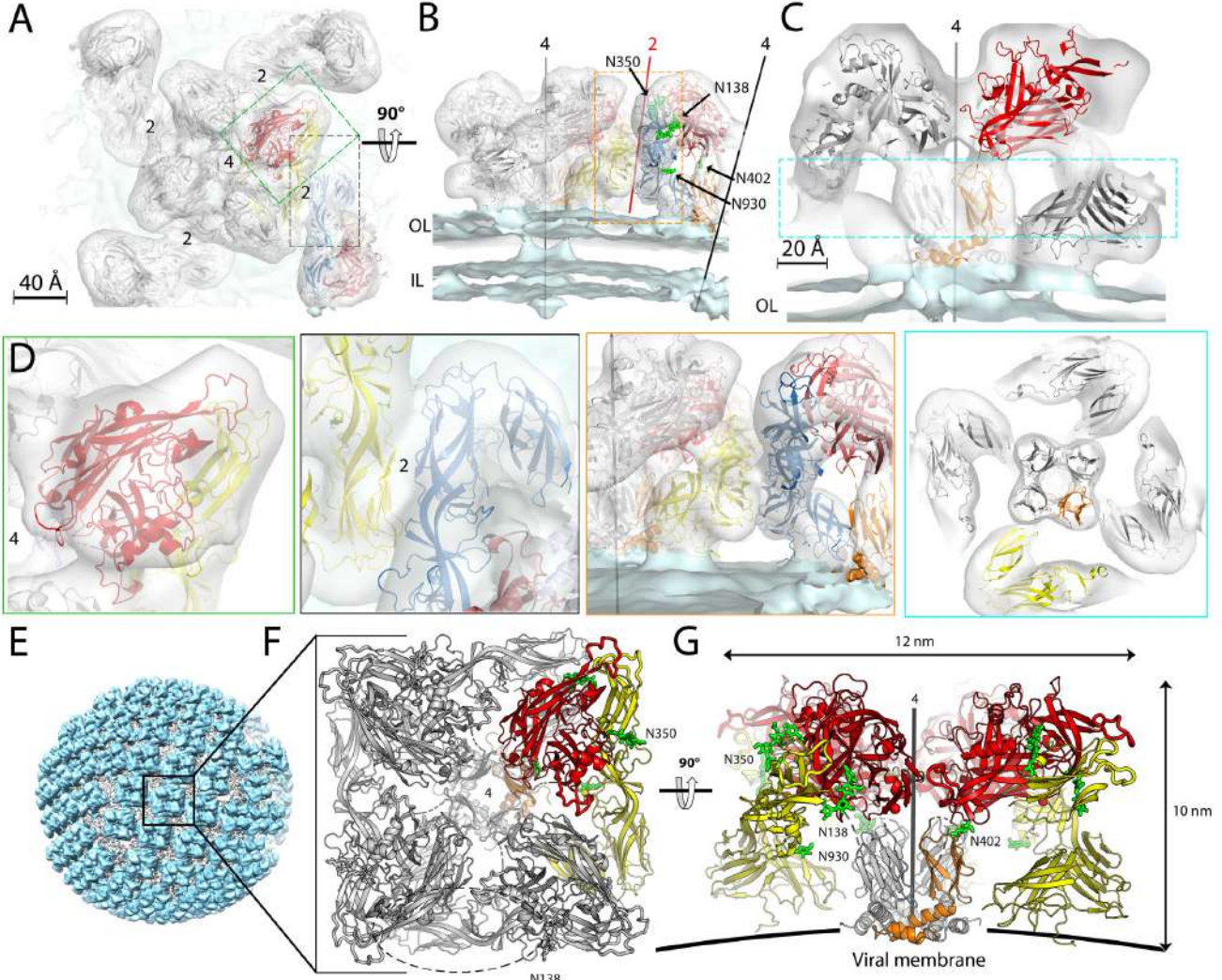

Figure 2

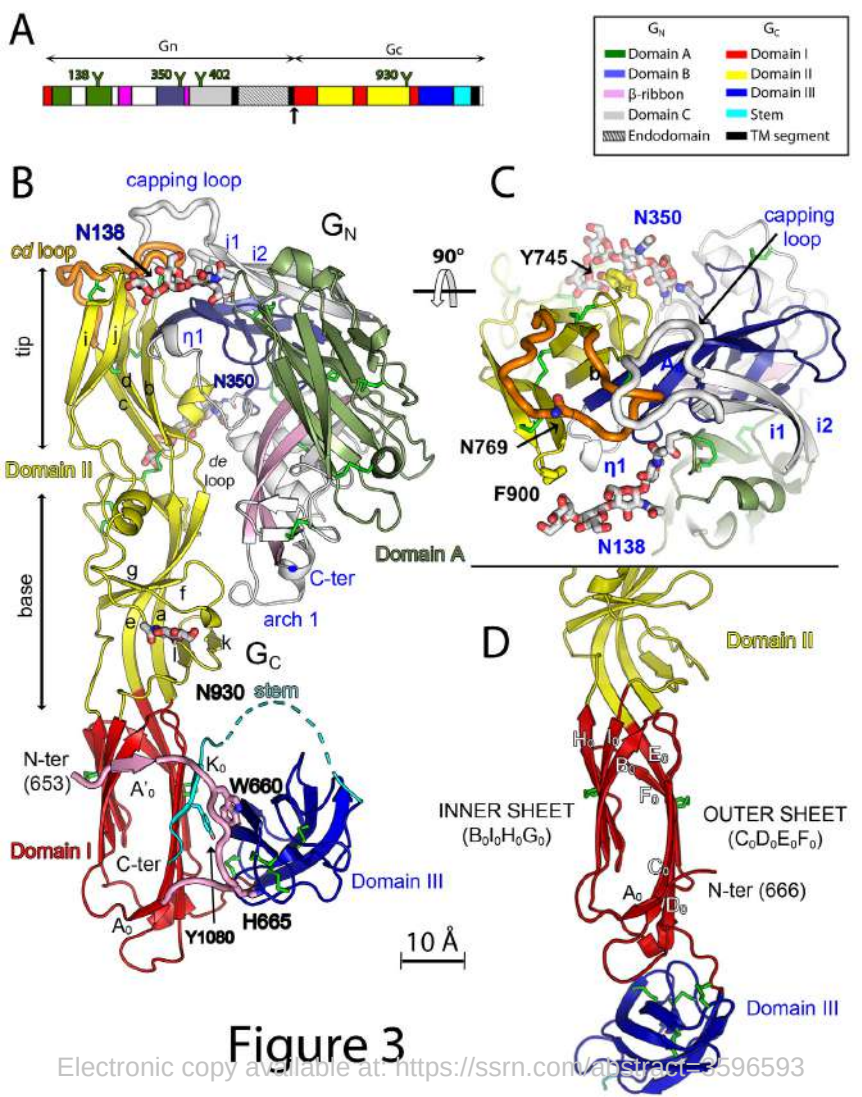

Figure 3

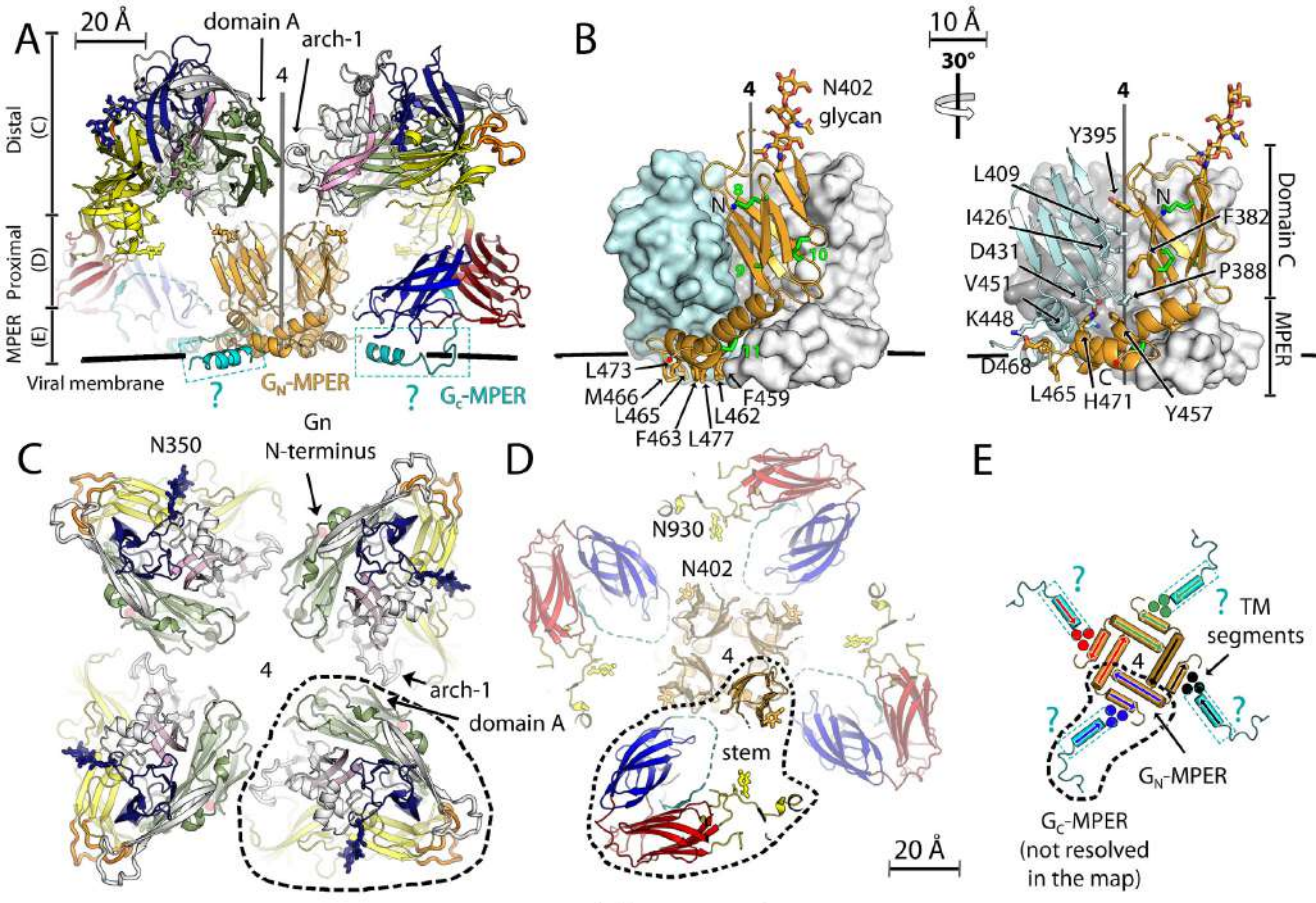

Figure 4

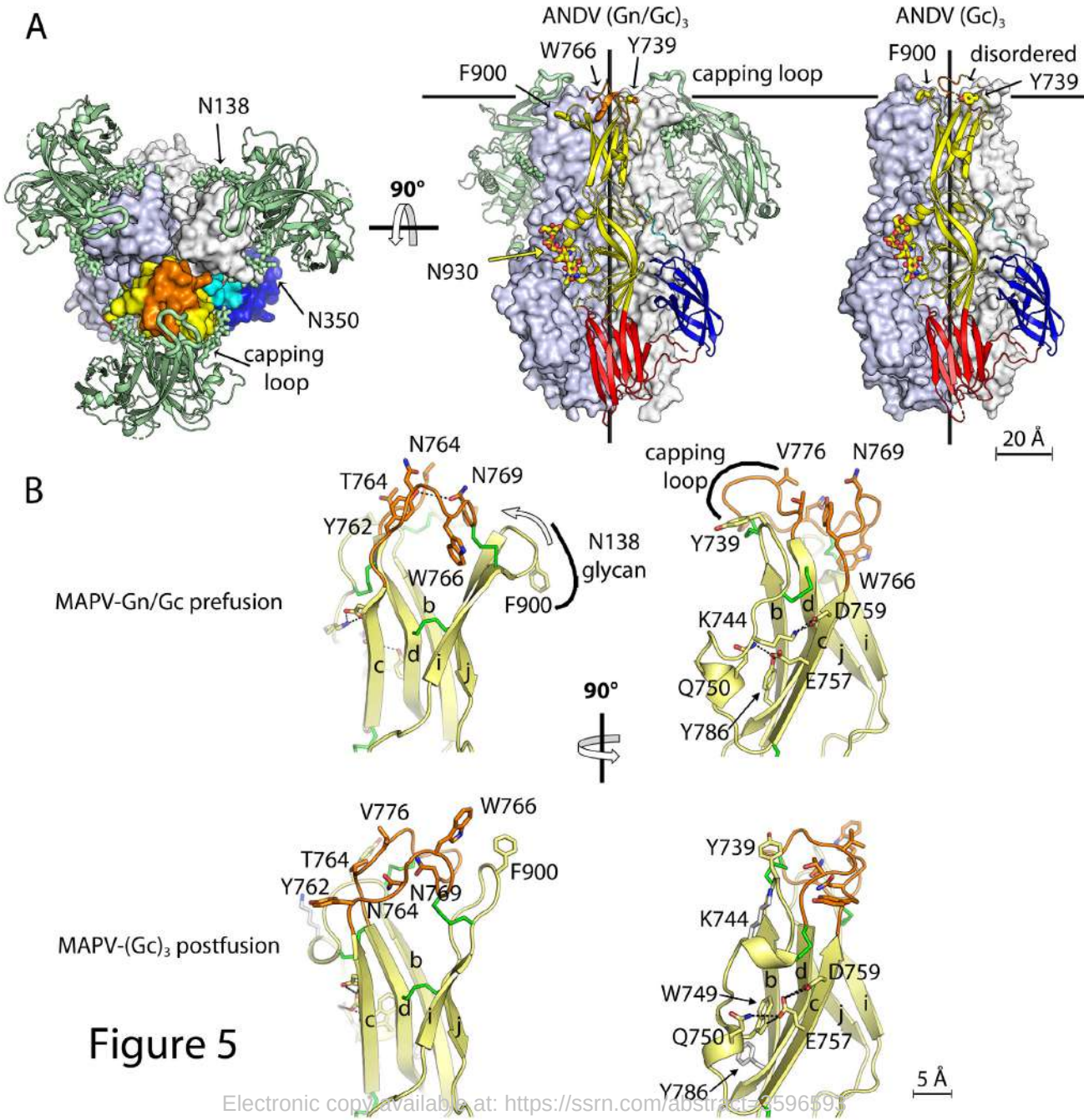

Figure 5

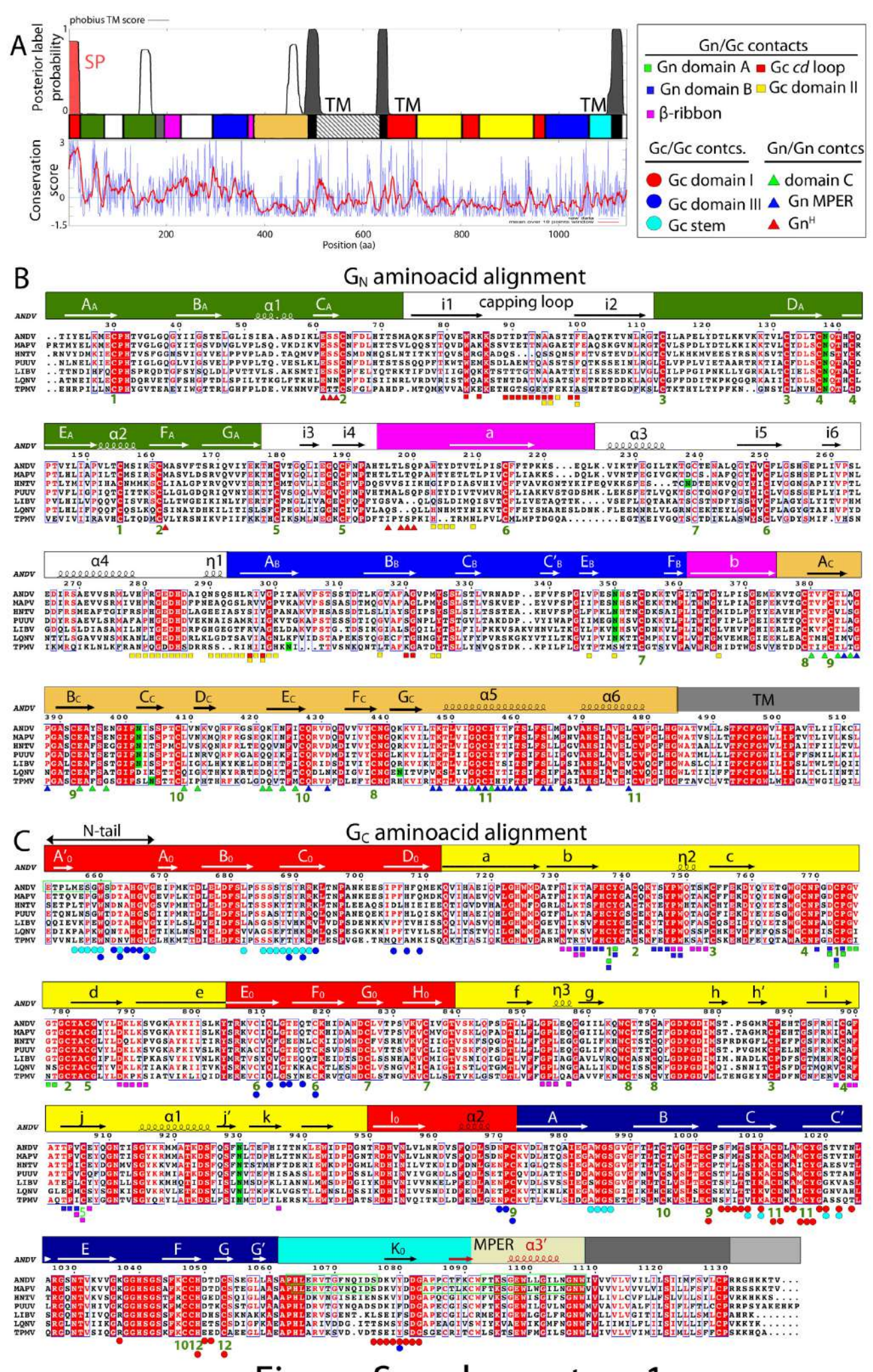

Figure Supplementary 1

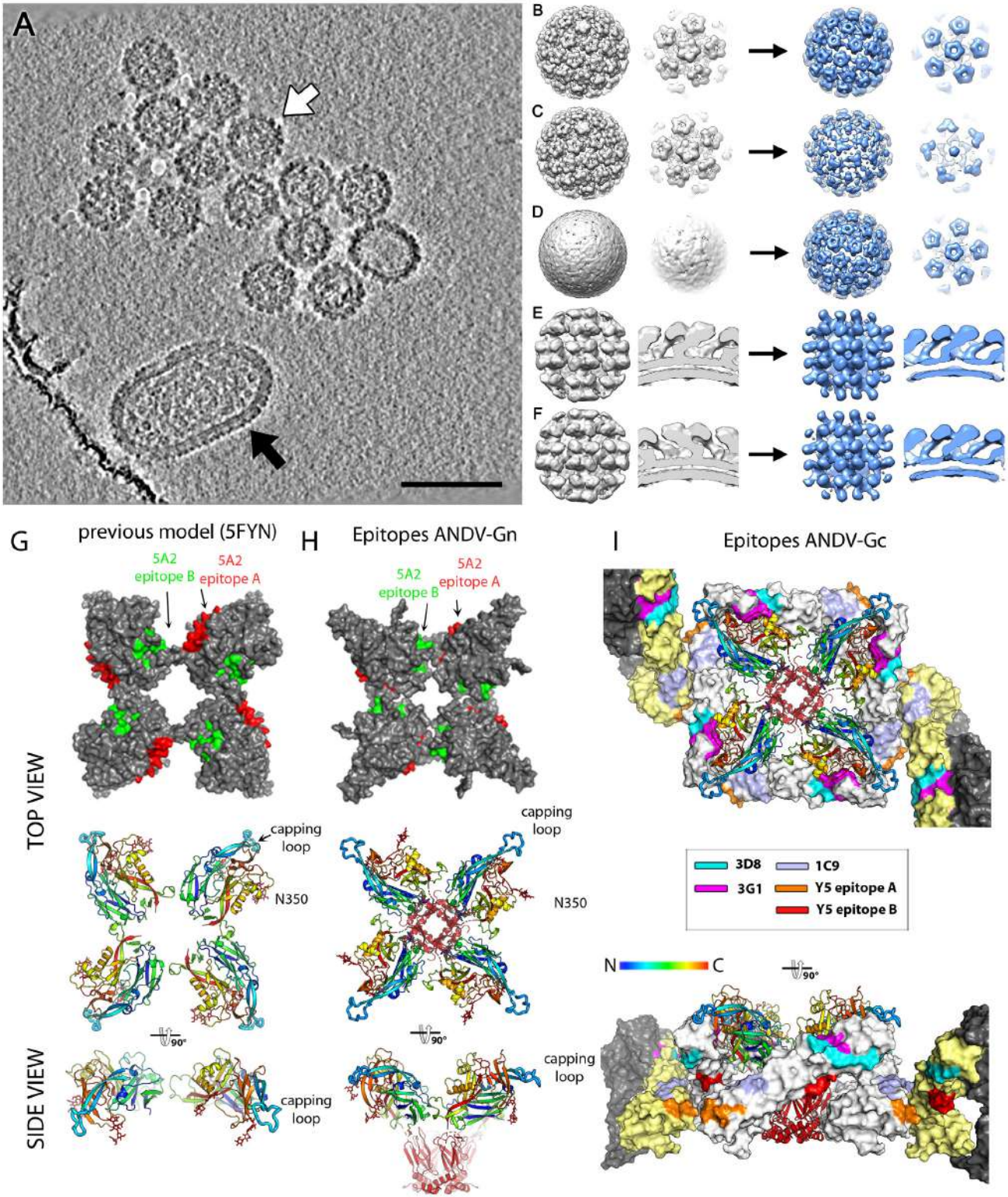

Figure Supplementary 2

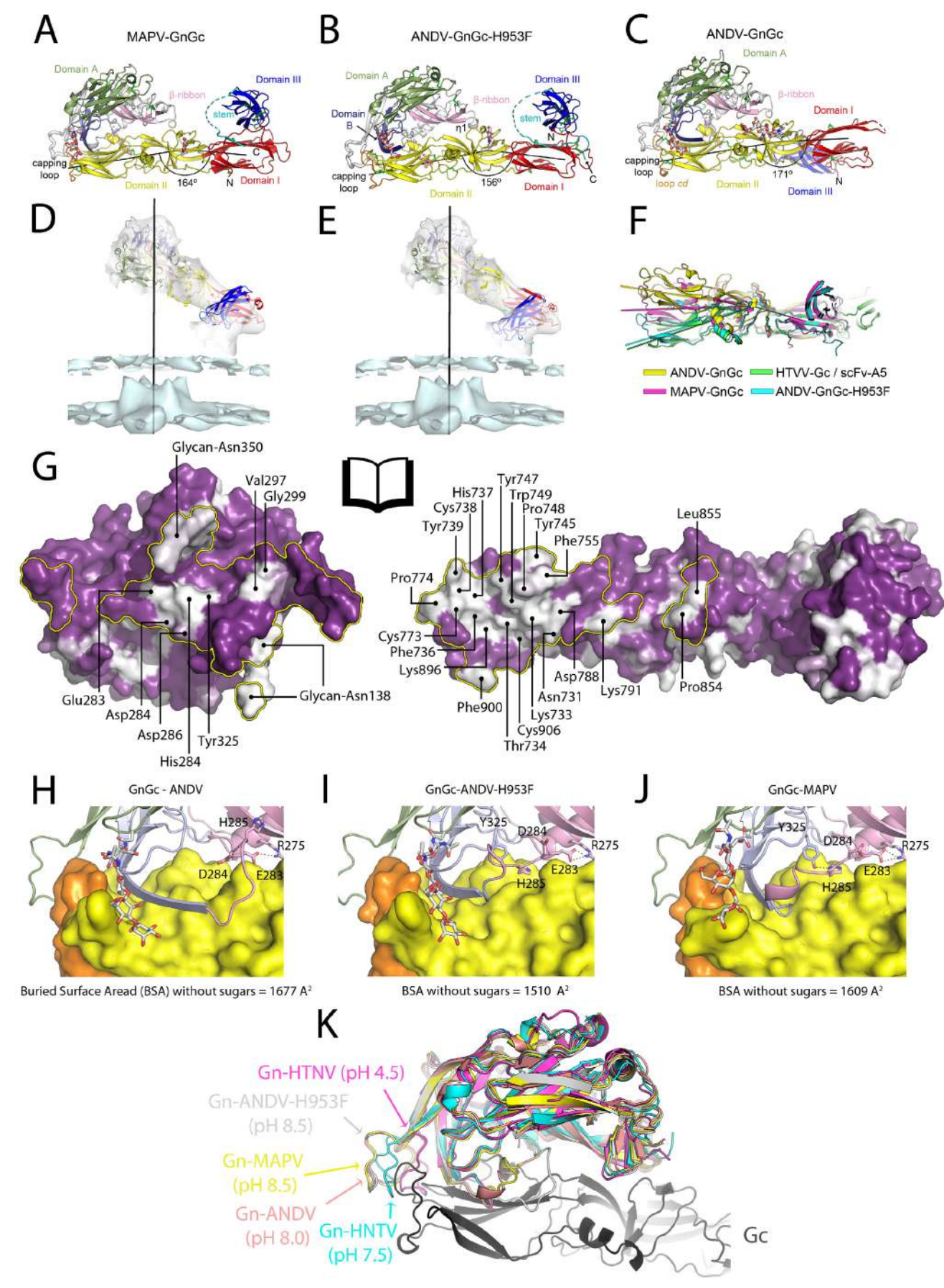

Figure Supplementary 3

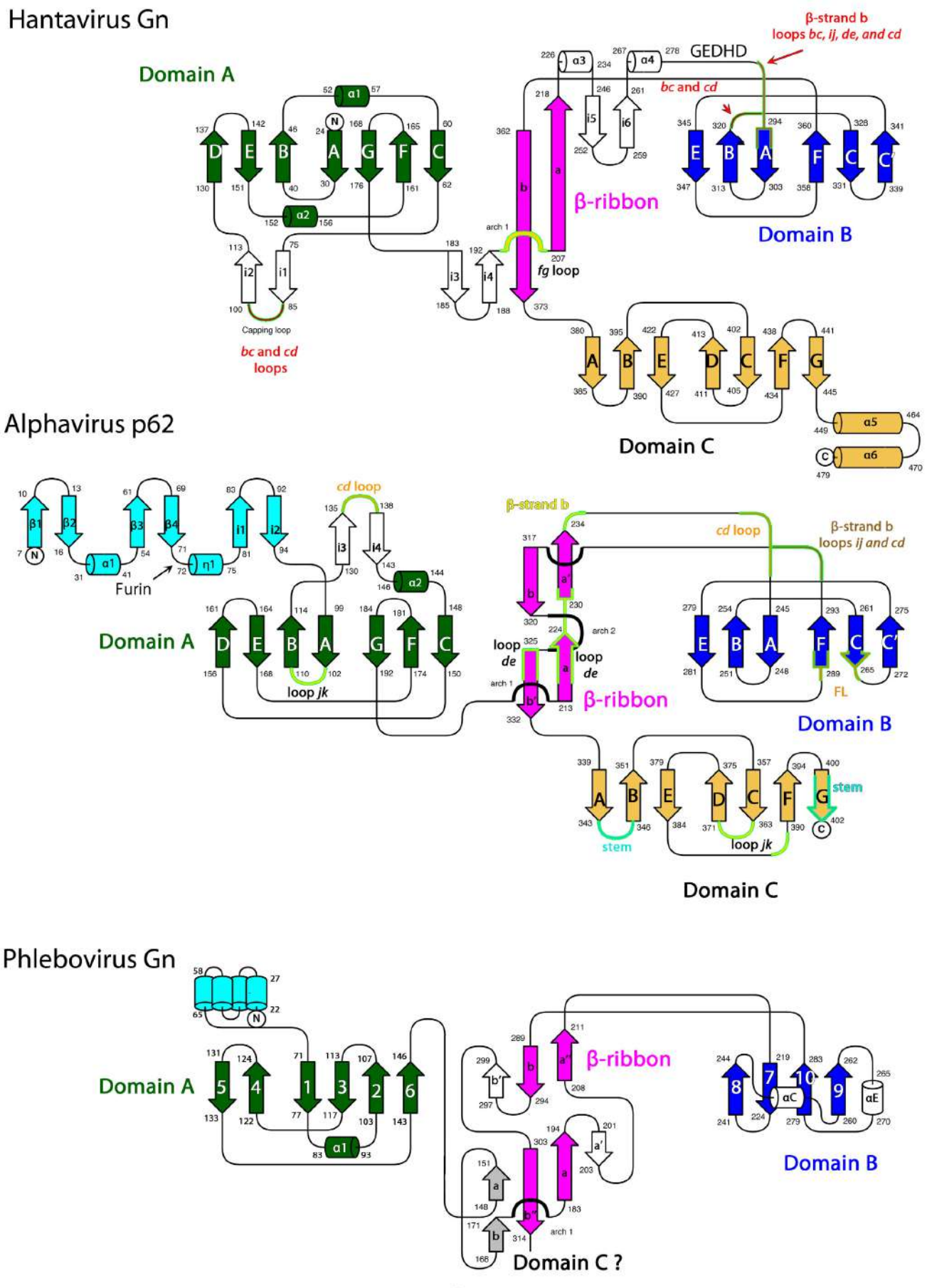

Figure Supplementary 4

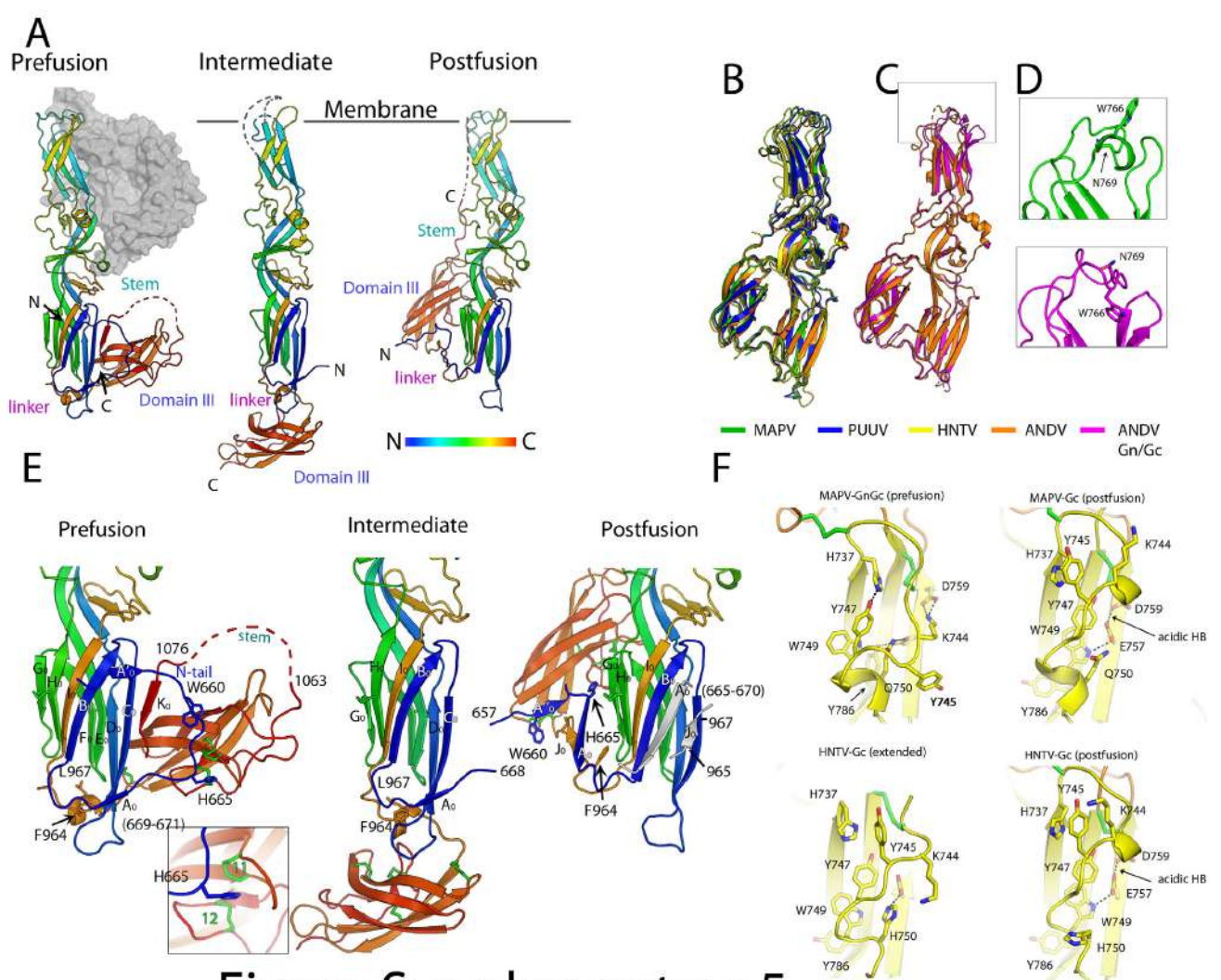

Figure Supplementary 5